Evolution of the magnetic and polaronic order of $Pr_{1/2}Ca_{1/2}MnO_3$ following an ultrashort light pulse

Sangeeta Rajpurohit,[1] Christian Jooss,[2] and Peter E. Blöchl[1,3,*]

[1]*Institute for Theoretical Physics, Clausthal University of Technology, Clausthal-Zellerfeld, Germany*

[2]*Institute for Material Physics, Georg-August-Universität Göttingen, Göttingen, Germany*

[3]*Institute for Theoretical Physics, Georg-August-Universität Göttingen, Göttingen, Germany*

(Received 22 October 2019; revised 9 March 2020; accepted 28 April 2020; published 2 July 2020)

The dynamics of electrons, spins, and phonons induced by optical femtosecond pulses has been simulated for the polaronic crystal $Pr_{1/2}Ca_{1/2}MnO_3$. The model used for the simulation has been derived from *first-principles* calculations. The simulations reproduce the experimentally observed melting of charge and orbital order with increasing fluence. The loss of charge order in the high-fluence regime induces a transition to a ferromagnetic metal. At low fluence, the dynamics is deterministic and coherent phonons are created by the repopulation of electronic orbitals, which are strongly coupled to the phonon degrees of freedom. In contrast to the low-fluence regime, the magnetic transitions occurring at higher fluence can be attributed to a quasithermal transition of a cold-plasma-like state with hot electrons and cold phonons and spins. The findings can be rationalized in a more complete picture of the electronic structure that goes beyond the simple ionic picture of charge order.

DOI: 10.1103/PhysRevB.102.014302

I. INTRODUCTION

Unlike traditional spectroscopy, ultrafast pump-probe spectroscopy is a powerful tool to dynamically track the interactions in a strongly correlated system. Specifically, manganites are a suitable model system because different types of correlations between electrons, spins, and phonons have similar strength. A number of different electronic ground states can be realized just by changing temperature or doping. In these materials, high-resolution ultrafast pump-probe spectroscopy experiments have unraveled interesting physical effects, such as photoinduced phase transitions [1–3] and transient "hidden" phases [4].

In manganite perovskites, a growing number of ultrafast experiments provide access to the dynamics on different timescales from femtoseconds to nanoseconds. The dynamics depends on the phase of the selected manganite as well as on the photon energy and intensity of the pump pulse. In $GdSrMnO_3$ close to half-doping, a photoinduced transition from a charge-order phase to a ferromagnetic metallic phase within 200 fs has been observed [2]. An ultrafast metal-insulator transition has been induced in $Pr_{0.7}Ca_{0.3}MnO_3$ by selectively exciting phonon modes at 625 cm^{-1} [5]. On shorter timescales, coherent oscillations in the sample resistance in the insulator-to-metal dynamics with 30 THz are interpreted as orbital waves [6]. Several ultrafast optical-pump terahertz-probe studies in manganites focused on probing the nature of the quasiparticles and their dynamics within a given phase [5–7].

Optical pump-probe experiments suggest a two-component relaxation process in $Nd_{0.5}Sr_{0.5}MnO_3$ [8] and $La_{0.7}Ca_{0.3}MnO_3$ [9–11]. In the paramagnetic insulating phase of $La_{0.7}Ca_{0.3}MnO_3$, the fast component <1 ps involves thermalization of electronic subsystem and its energy redistribution with the lattice subsystem. The slower component on the 20–200 ps timescale, with a T_c-dependent lifetime, is attributed to the spin-lattice relaxation [3,10,11].

Recently, long-lived polaron-type optical excitations with lifetime of 1–2 ns are observed in the charge-ordered phase of $Pr_{0.7}Ca_{0.3}MnO_3$ [7]. Another long-lived intermediate state, with a mixture of ferromagnetic metallic and charge-ordered nanoscale domains, is observed in $La_{0.325}Pr_{0.3}Ca_{0.375}MnO_3$ [12]. Depending on the phase and excitation intensity, coherent acoustic phonons as well as oscillating strain waves are observed on timescales of several 10 ps [13,14]; for manganites, see [15].

The goal of this work is to augment previous experimental studies with a detailed description of the microscopic processes occurring during the first few picoseconds. For this purpose, we perform simulations that are verified by comparing our findings with experimental observations. The work presented here is parameter free in the sense that the model parameters have been extracted from first-principles calculations [16].

We simulate the photoexcitation of $Pr_{1/2}Ca_{1/2}MnO_3$ by a femtosecond light pulse and the subsequent relaxation of the magnetic and polaronic microstructure for the first few picoseconds. Ehrenfest dynamics [17] is adopted to propagate wave functions, spins, and atoms. Peierls substitution has been employed to incorporate the external light pulse. A systematic

*peter.bloechl@tu-clausthal.de.

study is performed to investigate the relaxation process by varying the intensity of the light pulse.

The paper is organized as follows: The methods of the paper are covered in Sec. II: the tight-binding model used for the electron, spin, and phonon degrees of freedom is described first, followed by the dynamical equations of motion, the treatment of the optical excitation, and quantities used in the analysis. In Sec. III, we revisit the ground state of $Pr_{1/2}Ca_{1/2}MnO_3$, which experiences the optical excitation. Thereafter, we describe in Sec. IV the results of our simulations and discuss the underlying mechanisms. Finally, we summarize the findings in Sec. V.

II. METHODS

A. Tight-binding model

To investigate the electronic, atomic, and magnetic microstructure of manganites, we employ a tight-binding model [18–20]. The selection of energy terms and the parameter values have been extracted from the first-principles calculations [16].

The model describes the correlations between electron, spin, and phonon degrees of freedom. The explicit electronic degrees of freedom describe the Mn d electrons with e_g character. The spin degrees of freedom describe the three majority-spin d orbitals of each Mn ion with t_{2g} character. The phonon degrees of freedom are two Jahn-Teller active vibration modes and one breathing mode of each MnO_6 octahedron. In addition, we allow for a global expansion of the lattice.

The potential-energy functional of the system is

$$E_{\text{pot}} = E_e + E_S + E_{ph} + E_{e\text{-}ph} + E_{e\text{-}S}, \tag{1}$$

where the E_e, E_S, and E_{ph} are the energies of the isolated electronic, spin, and phonon subsystems, respectively. $E_{e\text{-}ph}$ is the electron-phonon coupling of Mn e_g electrons with the Jahn-Teller active modes as well as with the breathing mode of the MnO_6 octahedra. $E_{e\text{-}S}$ is Hund's coupling between the e_g electrons and the spins of the Mn t_{2g} electrons.

Our model avoids the common infinite Hund's-coupling limit [21] and uses a more realistic description with explicit minority-spin electrons and a fully noncollinear treatment of the electron spin. Furthermore, we include the strong cooperativity of Jahn-Teller distortions and octahedral breathing modes by expressing them in terms of the explicit oxygen positions, which are shared each by two adjacent MnO_6 octahedra.

The Mn e_g electrons are described by a Slater determinant formed by the one-particle wave functions $|\psi_n\rangle$. The latter are expressed as superposition of local orbitals $|\chi_{\sigma,\alpha,R}\rangle$ with complex-valued coefficients $\psi_{\sigma,\alpha,R,n}$:

$$|\psi_n\rangle = \sum_{\sigma,\alpha,R} |\chi_{\sigma,\alpha,R}\rangle \psi_{\sigma,\alpha,R,n}. \tag{2}$$

The local orbital $|\chi_{\sigma,\alpha,R}\rangle$ is a spin orbital with e_g character at the Mn site R. It is a spin eigenstate with spin $\sigma \in \{\uparrow, \downarrow\}$ and spatial orbital character $\alpha \in \{a, b\}$ (where $a{=}d_{x^2-y^2}$ and $b{=}d_{3z^2-r^2}$) [16]. The wave functions are Pauli spinor wave functions that account for the noncollinear nature of the magnetization.

The three majority-spin t_{2g} electrons of a Mn site with site index R are described by a spin vector $\vec{S}_R$ [16]. The two Jahn-Teller active phonon modes $Q_{2,R}$ and $Q_{3,R}$ for each MnO_6 octahedron as well as the breathing mode $Q_{1,R}$ are expressed by the displacements of oxygen ions along the Mn-O-Mn bridge using Eq. (22) of [16].

B. Dynamics

The dynamics of the optical excitation and its relaxation processes are described by Ehrenfest dynamics [17,22]: that is, the electrons evolve under the time-dependent Schrödinger equation, while the atoms are treated as classical particles and obey Newton's equations of motion:

$$i\hbar\partial_t \psi_{\sigma,\alpha,R,n} = \frac{\partial E_{\text{pot}}}{\partial \psi^*_{\sigma,\alpha,R,n}}, \tag{3}$$

$$\partial_t S_{j,R} = \frac{2m_S}{\hbar} \vec{B}_R \times \vec{S}_R, \tag{4}$$

$$M_O \partial_t^2 R_j = -\frac{\partial E_{\text{pot}}}{\partial R_j}. \tag{5}$$

R_j are the structural degrees of freedom of the oxygen ions and M_O is their mass. m_S is the absolute value of the magnetic moment of the t_{2g} spins and the quasimagnetic field $\vec{B}_R$ is

$$B_{j,R} = \frac{3\hbar}{2m_S} \frac{\partial E}{\partial S_{j,R}}. \tag{6}$$

Further details are given in Appendices A and B. We also allowed for a strain dynamics, which does not have notable consequences on the results presented here. For the sake of completeness, it is described in Appendix C.

C. Light pulse

The light pulse is described by a spatially homogeneous, but time-dependent, electromagnetic field (see Appendix D)

$$\vec{E}(t) = \vec{e}_A \omega \,\text{Im}(A_0^* e^{i\omega t}) g(t), \tag{7}$$

where A_0 is the amplitude of the vector potential and $\hbar\omega$ is the photon energy. c is the speed of light. The polarization of the electric field and of the vector potential is the unit vector $\vec{e}_A$. The temporal profile of the laser pulse is described by a Gaussian

$$g(t) = \frac{1}{\sqrt[4]{\pi c_w^2}} e^{-\frac{t^2}{2c_w^2}}. \tag{8}$$

The intensity, which is proportional to $|g(t)|^2$, has the full width at half-maximum (FWHM) of $2c_w\sqrt{\ln 2}$. The light pulse is implemented with the Peierls-substitution method [23,24]. Details are given in Appendix D.

D. Parameters of the simulation

Table I summarizes the relevant parameters used in this paper. We use a Cartesian coordinate system with the coordinate axes $\vec{e}_x$, $\vec{e}_y$, and $\vec{e}_z$ pointing along the Mn-Mn nearest-neighbor distances. The vectors $\vec{e}_j$ are defined with length 1.

TABLE I. Simulation parameters. For explanation, see text.

k grid	$1\times1\times1$
Supercell	$N_x\times N_y\times N_z = 8\times8\times4$
Mn sites per unit cell	$N_{\text{Mn}} = 256$
O sites per unit cell	$N_{\text{O}} = 768$
Mn-Mn spacing	$d_{\text{Mn-Mn}} = 3.84$ Å
Time step	$\Delta_t = 0.040(4\pi\epsilon_0)^2\hbar^3/(m_e e^4)$ $= 0.97\times10^{-18}$ s
Oxygen mass	$M_{\text{O}} = 15.998$ u
Fictitious cell mass	$M_g = 8.0\times10^{10}$ m_e
Photon energy	$\hbar\omega = 1.17$ eV
Pulse length (FWHM)	$2\sqrt{\ln 2}c_w = 100$ fs
Polarization	$\vec{e}_A = (\vec{e}_x + \vec{e}_y)/\sqrt{2}$
Initial tetragonal distortion	$g_x = g_y = 1.0388$, $g_z = 1.0077$

The Mn-Mn nearest-neighbor vectors are $g_x d_{\text{Mn-Mn}}\vec{e}_x$, $g_y d_{\text{Mn-Mn}}\vec{e}_y$, and $g_z d_{\text{Mn-Mn}}\vec{e}_z$ with $d_{\text{Mn-Mn}}$ from Table I and scale factors g_x, g_y, and g_z. With N_x, N_y, and N_z, we denote the number of Mn sites in each of the three spatial directions in the supercell used in the calculation.

To describe perovskites, one usually refers to the lattice vectors of *Pbnm* unit cell, a nonstandard setting of space group 62. The lattice vectors $\vec{a}$, $\vec{b}$, and $\vec{c}$ of the *Pbnm* unit cell are

$$\begin{aligned}\vec{a} &= (g_x\vec{e}_x - g_y\vec{e}_y)d_{\text{Mn-Mn}},\\ \vec{b} &= (g_x\vec{e}_x + g_y\vec{e}_y)d_{\text{Mn-Mn}},\\ \vec{c} &= 2g_z\vec{e}_z d_{\text{Mn-Mn}}.\end{aligned} \tag{9}$$

The pulse length has been chosen consistent with the laser pulses used in ultrafast pump-probe experiments [7].

The parameters of the tight-binding model are summarized in an earlier publication [16]. In the present model, we have adjusted some of these values as follows: The antiferromagnetic coupling has been set to $J_{\text{AF}} = 15$ meV rather than $J_{\text{AF}} = 14$ meV. The restoring force constant for the breathing mode has been set to $k_{br} = 9.04$ eV/Å^2 rather than 10.346 eV/Å^2 in order to $\sqrt{Q_2^2 + Q_3^2}/Q_1$ obtained with our first-principles calculations for $PrMnO_3$ (A type).

E. Diffraction patterns

In order to link our results with diffraction experiments, we inspect the intensities of diffraction for charges, orbitals, and spins.

The intensity of diffraction of an observable $\hat{X}$, such as number of electrons, orbital occupations, or spins, with density $x(\vec{r})$ is [25]

$$I_X(\vec{q}) := I_{X,0}(\vec{q})\left|\int_V d^3r\, x(\vec{r})e^{-i\vec{q}\vec{r}}\right|^2, \tag{10}$$

where the integration is performed over the illuminated sample volume V. $I_{X,0}(\vec{q})$ is the intensity of diffraction of a point scatterer $x(\vec{r}) = X\delta(\vec{r})$.

For a periodic lattice of atom-centered distributions $x(\vec{r}) = \sum_{R,\vec{t}} x_R(\vec{r} - \vec{R}_R - \vec{t})$, the intensity of diffraction is

$$I_X(\vec{q}) = I_{X,0}(\vec{q})N_{\in V}\Omega_G\sum_G \delta(\vec{q} - \vec{G})C_X(\vec{G}) \tag{11}$$

with the correlation function [26]

$$C_X(\vec{G}) = \frac{1}{N}\left|\sum_{R=1}^{N} e^{-i\vec{G}\vec{R}_R}X_R(\vec{G})\right|^2. \tag{12}$$

The distributions $x_R(\vec{r})$ are placed at the lattice sites $\vec{R}_R + \vec{t}$, where $\vec{R}_R$ is the position of an atom inside the first unit cell and $\vec{t}$ is the lattice translation vector of a specific unit cell. N is the number of atoms in the unit cell, Ω_T is the unit-cell volume, $\Omega_G = (2\pi)^3/\Omega_T$ is the unit-cell volume of the reciprocal lattice, and $\vec{G}$ are the corresponding general reciprocal-lattice vectors. $N_{\in V}$ is the number of sites in the illuminated region. $X_R(\vec{q}) := \int d^3r\, x_R(\vec{r})e^{-i\vec{q}\vec{r}}$ is the form factor of x_R. Note that the correlation function is meaningful only at the reciprocal-lattice vectors $\vec{G}$.

Specifically, we address the following diffraction patterns:

(i) The charge-order correlation function [26]

$$C_Q(\vec{G}) := \frac{1}{N}\left|\sum_{R=1}^{N} e^{i\vec{G}\vec{R}_R}(n_R - \langle n\rangle)\right|^2 \tag{13}$$

probes the deviation of the electron density from its mean value, i.e., $X_R = n_R - \langle n\rangle$, where $n_R = \sum_{\alpha,\sigma}\rho_{\sigma,\alpha,R,\sigma,\alpha,R}$ is the number of e_g electrons on Mn site R and $\langle n\rangle = 1 - x$ with the doping $x = \frac{1}{2}$ is the average number of electrons on Mn sites. The one-particle-reduced density matrix

$$\rho_{\sigma,\alpha,R,\sigma',\alpha',R'} =: \sum_n f_n\psi_{\sigma,\alpha,R,n}\psi^*_{\sigma',\alpha',R',n} \tag{14}$$

is given by the wave-function coefficients $\psi_{\sigma,\alpha,R,n}$ and the occupations f_n.

(ii) The orbital-order correlation function

$$C_O(\vec{G}) := \frac{1}{N}\left|\sum_{R=1}^{N} e^{i\vec{G}\vec{R}_R}(n_{x,R} - n_{y,R})\right|^2 \tag{15}$$

probes difference between the orbital occupations $X_{j,R} = n_{x,R} - n_{y,R}$, where

$$n_{j,R} = \sum_{\alpha,\beta}\langle\theta_j|\chi_\alpha\rangle\left(\sum_\sigma \rho_{\sigma,\alpha,R,\sigma,\beta,R}\right)\langle\chi_\beta|\theta_j\rangle \tag{16}$$

are calculated for the set of orthonormal orbitals $|\theta_j\rangle$ with $j \in \{x, y\}$, which are nearly axial in the x, respectively the y direction. These orbitals are defined in terms of the original basis states $|d_{x^2-y^2}\rangle$ and $|d_{3z^2-r^2}\rangle$ as

$$|\theta_x\rangle := (|d_{3z^2-r^2}\rangle - |d_{x^2-y^2}\rangle)\frac{1}{\sqrt{2}} \tag{17}$$

and

$$|\theta_y\rangle := -(|d_{3z^2-r^2}\rangle + |d_{x^2-y^2}\rangle)\frac{1}{\sqrt{2}}. \tag{18}$$

We skip spin and site indices of the Wannier-type orbitals for scalar products, where they are identical.

(iii) The spin-correlation function [26]

$$C_S(\vec{G}) := \frac{1}{N}\left|\sum_{R=1}^{N} e^{i\vec{G}\vec{R}_R}(\vec{S}_R + \vec{s}_R)\right|^2 \tag{19}$$

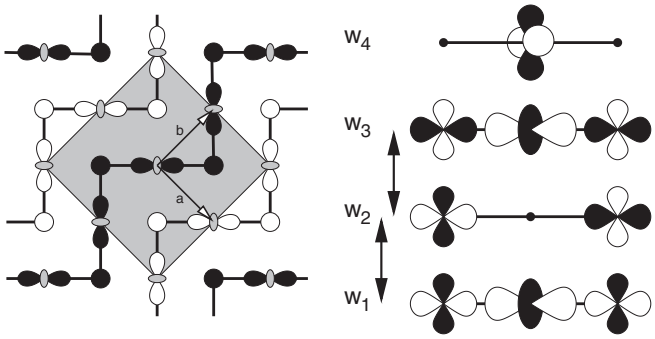

FIG. 1. Left: CE-type magnetic order and orbital order in the *ab* plane of the ground state of $Pr_{1/2}Ca_{1/2}MnO_3$. Black and white symbols indicate up and down spins. The orbital-polarized central orbitals are indicated by a $d_{3z^2-r^2}$ orbital symbol in the corresponding direction. The corner sites have no orbital polarization and are indicated by circles. The gray square indicates the magnetic unit cell of the material in the *ab* plane. Also shown are the lattice vectors *a* and *b* of the orthorhombic *Pbnm* unit cell. Right: Wannier-type orbitals along a trimer of the zigzag chains of the CE-type magnetic structure. The sign of the orbital lobes are indicated by black and white. The Wannier-type orbitals are orthogonal within and between trimers. The arrows connect orbitals with dipole-allowed transitions. Transitions between all other orbital pairs within and between trimers are dipole forbidden. The orbital $|w_1\rangle$ in the majority-spin direction is filled. The optical excitation lifts electrons from $|w_1\rangle$ to $|w_2\rangle$ in the majority-spin direction.

probes the total spin $\vec{X}_R = \vec{S}_R + \vec{s}_R$ of the Mn sites, where $\vec{S}_R$ is the spin of the t_{2g} electrons and $\vec{s}_R$ is the spin of the e_g electrons at Mn site *R*.

In order to account for the blurring of the diffraction peaks due to fluctuations, we included for the time-dependent spin correlation functions, in Figs, 13, 19, and 23, the contribution from a $(3 \times 3 \times 3)$ set of reciprocal lattice vectors of the supercell centered at the specified reciprocal-lattice vector.

III. EQUILIBRIUM

Before investigating the optically induced dynamics, let us remind of the salient features of the spin, charge, orbital, and lattice order of $Pr_{1/2}Ca_{1/2}MnO_3$ in equilibrium. The low-temperature phase serves as initial state for the excitation and it determines the time evolution of the system.

$Pr_xCa_{1-x}MnO_3$ has a perovskite lattice formed by a network of corner-sharing MnO_6 octahedra. Large cations such as Ca^{2+} and Pr^{3+} fill the voids in-between the octahedra. The octahedral network distorts to optimize the Coulomb energy between the ions, which results in a characteristic pattern of the octahedral tilts. This tilt pattern fits into the orthorhombic *Pbnm* unit cell, which holds four octahedra.

The Mn ions occur in the formal Mn^{4+} and Mn^{3+} oxidation states, with spin-aligned *d* electrons on each Mn site. The additional electron of Mn^{3+} produces a Jahn-Teller distortion, which is highly cooperative.

At half-doping, $Pr_xCa_{1-x}MnO_3$ has a low-temperature phase, which is described as charge and orbital ordered [27–29]. The low-temperature phase of $Pr_{1/2}Ca_{1/2}MnO_3$ is shown schematically in Fig. 1. It has a CE-type antiferromagnetic order exhibiting ferromagnetic zigzag chains in the *ab* plane, which proceed along the *b* direction. These zigzag chains are antiferromagnetically coupled among each other. Along the zigzag chain, we can distinguish alternating central and corner sites. The central sites are described formally as Mn^{3+} ions and exhibit Jahn-Teller distortion, while the corner sites are formally Mn^{4+} ions with a negligible Jahn-Teller distortion.

TABLE II. Typical diffraction patterns. The diffraction spots are shown for various spin orders according to the notation of Wollan [27] as well as for charge and orbital diffraction of the CE-type low-temperature structure of $Pr_{1/2}Ca_{1/2}MnO_3$. (h, k, l) are the relative coordinates in the reciprocal lattice of the orthorhombic *Pbnm* setting. h, k, l are integer unless mentioned otherwise.

Spin	$h+k$		l
B type	Even integer		Even integer
A type	Even integer		Odd integer
C type	Odd integer		Even integer
G type	Odd integer		Odd integer
CE type	h	k	l
Spin	Half-integer not integer	Half-integer or integer	Odd integer
Charge	$h+k=$ odd integer		Even integer
Orbital	Integer	Half-integer not integer	Even integer

A. Diffraction patterns

A transition at 250 K is attributed to the emergence of charge and/or orbital order [29] from a disordered polaron distribution at higher temperatures. The charge and orbital order has been explored experimentally by x-ray diffraction of the Mn *K* edge [30].

The diffraction patterns for the low-temperature phase are listed under the header CE-type in Table II. The diffraction peaks are quoted as relative coordinates (h, k, l) of the reciprocal lattice vectors in the setting of the orthorhombic (*Pbnm*) crystal structure obtained at room temperature.

Zimmermann *et al.* [30] exploited that the diffraction spots of charge and orbital order can be distinguished when scanning $(h, k, l) = (0, k, 0)$ along the *b* direction, the direction of the zigzag chain. The dominant peaks of the Mn *K* edge with even integer *k* are due to the pseudocubic atomic lattice of Mn sites. The charge order introduces additional diffraction peaks at odd integer *k*, and the orbital order produces diffraction spots at half-integer (but not integer) values of *k*, as shown in Fig. 2 and listed in Table II. At 175 K, $Pr_{1/2}Ca_{1/2}MnO_3$ undergoes a Néel transition. Neutron-diffraction studies [29] identify the magnetic lines characteristic for the CE-type spin order for $Pr_{1/2}Ca_{1/2}MnO_3$.

Our simulations reproduce the diffraction patterns due to charge, orbital, and spin order for the CE-type ground state as shown in Fig. 2. The diffraction spots of other magnetic orders listed in Table II will be used to characterize the evolution of the magnetic order following the light pulse: B type refers to a pure ferromagnet, A type refers to ferromagnetic planes that are stacked antiferromagnetically

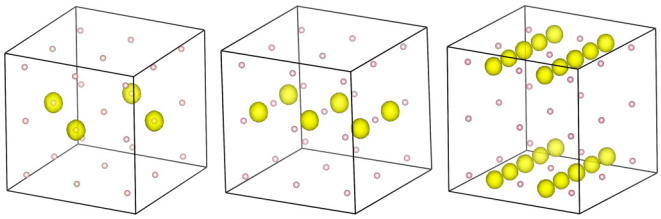

FIG. 2. Diffraction patterns for charge order (left), orbital order (middle), and spin order (right) of the CE-type low-temperature phase of $Pr_{1/2}Ca_{1/2}MnO_3$. The a axis points right, the b axis toward the back, and the c axis up. The small white spheres indicate points with integer h, k, l in the *Pbnm* setting. Reciprocal space is shown for $h, k, l \in [-1.25, 1.25]$.

in the c direction, C type refers to ferromagnetic Mn lines running along the c direction, which are antiferromagnetically aligned with respect to neighboring strands. In a G-type antiferromagnet, the Mn sites are antiferromagnetic with respect to all their neighbors. The magnetic orders can also be described by their wave vector of the magnetization. Expressed by the pseudocubic lattice formed by the Mn sites, the B-type order refers to $\vec{k} = \frac{\pi}{d_{\text{Mn-Mn}}}(0, 0, 0)$, A type refers to $\vec{k} = \frac{\pi}{d_{\text{Mn-Mn}}}(0, 0, 1)$, C type refers to $\vec{k} = \frac{\pi}{d_{\text{Mn-Mn}}}(1, 1, 0)$, and G type refers to $\vec{k} = \frac{\pi}{d_{\text{Mn-Mn}}}(1, 1, 1)$.

B. Charge order, orbital order, and Jahn-Teller distortions

The pattern of Jahn-Teller distortions in Fig. 1 has been attributed to checkerboardlike charge order in the *ab* plane with Mn^{3+} ions at the central sites of each segment and Mn^{4+} ions at the corner sites of the zigzag chains [28]. More recently, this picture of charge order has been challenged: Rather than deducing the charge state from the pattern of Jahn-Teller distortions, experimental techniques such as core level spectroscopy, (XANES, ELNES) and neutron diffraction measurements of the magnetic moments provide a more direct access to the charge on the ions. These experiments rule out a fully ionic picture and indicate the absence of a considerable charge disproportionation [29,31–34].

This seeming contradiction between atomic structure and charge distribution can be reconciled by considering orbital polarization [16]. A Mn ion has a complete orbital polarization, when only one of the two spatial e_g orbitals is occupied, while the other is empty. Hereby, the shape and spin orientation of the occupied orbital is not relevant. When both spatial e_g orbitals are equally occupied, the atom lacks orbital polarization.

To quantify the orbital polarization at site R, we determine the difference $|f^{\text{orb}}_{1,R} - f^{\text{orb}}_{2,R}|$ of the orbital occupations $f^{\text{orb}}_{\alpha,R}$, which are the eigenvalues of the spin-averaged local density matrix $\boldsymbol{\rho}^{\text{orb}}_R$ with matrix elements

$$\rho^{\text{orb}}_{\alpha,\beta,R} := \sum_{\sigma} \rho_{\sigma,\alpha,R,\sigma,\beta,R}. \tag{20}$$

The orbital polarization P_O is defined as

$$\begin{aligned} P_O &:= |f^{\text{orb}}_{1,R} - f^{\text{orb}}_{2,R}| \\ &= \sqrt{\left(\rho^{\text{orb}}_{a,a,R} - \rho^{\text{orb}}_{b,b,R}\right)^2 + 4\left|\rho^{\text{orb}}_{a,b,R}\right|^2}, \end{aligned} \tag{21}$$

where a and b denote the two Mn e_g orbitals.

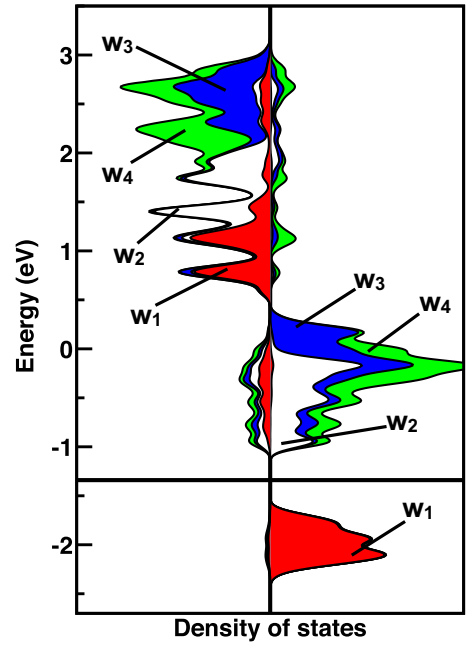

FIG. 3. Density of states of the ground state of $Pr_{1/2}Ca_{1/2}MnO_3$ projected on the Wannier-type states $|w_1\rangle$ (red), $|w_2\rangle$ (white), $|w_3\rangle$ (blue), and $|w_4\rangle$ (green). The axis of the majority-spin direction points right and that of the minority-spin direction points left.

Orbital polarization can be recognized indirectly via the resulting Jahn-Teller distortions. Mn ions without orbital polarization do not exhibit a Jahn-Teller distortion, irrespective of the number of electrons in the e_g shell. Hence, there is a direct link between Jahn-Teller distortions and orbital polarization. The connection to the charge order is, however, indirect. It is present only in the case of complete orbital polarization. This assumption is violated in $Pr_{1/2}Ca_{1/2}MnO_3$ [16]. The Jahn-Teller distortions of the corner sites are small, not because of their charge, but because of their lack of orbital polarization. The orbital polarization of the corner sites is small because Wannier-type orbitals from two segments of the zigzag chain contribute equally to the two e_g orbitals [16].

As shown earlier [16], the electronic structure of the low-temperature phase of $Pr_{1/2}Ca_{1/2}MnO_3$ can be rationalized using a specific set of Wannier-type states formed from the Mn e_g orbitals. These states, shown in Fig. 1, are localized on specific segments of the zigzag chains, which we denote, in the following, as trimers. The Wannier-type states are constructed as orthonormal eigenstates of a pseudosymmetry of a trimer, namely, three orthogonal mirror planes through the central Mn ion of a trimer. The functional form of the Wannier-type orbitals has been given in an earlier publication [16]. The requirements given above determine the Wannier-type orbitals up to a single parameter, which governs the charge disproportionation between central and corner sites. With a suitable choice of this parameter, the first Wannier-type state $|w_1\rangle$ describes the occupied states almost perfectly. This can be seen in Fig. 3, which shows that the occupied portion of the density of states can be attributed almost exclusively to $|w_1\rangle$. To be specific, the one-particle-reduced density matrix

of the e_g states is well described by

$$\rho_{\sigma,\alpha,R,\sigma',\beta,R'} = \sum_m \langle \chi_{\sigma,\alpha,R} | w_{\sigma_m,1,m} \rangle \delta_{\sigma,\sigma_m} \delta_{\sigma',\sigma_m} \times \langle w_{\sigma_m,1,m} | \chi_{\sigma',\beta,R'} \rangle, \quad (22)$$

where $|w_{\sigma,\alpha,m}\rangle$ is a Wannier-type orbital with spin σ, spatial type j with $j = \{1, 2, 3, 4\}$ according to Fig. 1, and the index m specifying a particular trimer. σ_m denotes the majority-spin direction of the trimer with index m.

In our model calculations, the charge on the central site is $3.75e$ and that of the corner site is $3.25e$, which corresponds to a charge disproportion of $q/e = 3.5 \pm \delta$ with $\delta = 0.25$. This value lies within the range of values obtained from various experimental probes as discussed earlier [16].

The shape of the orbital $|w_1\rangle$ is responsible for the orbital order with strong orbital polarization on the central size and negligible orbital polarization on the corner sites. Thus, the electronic structure is consistent with both the observed Jahn-Teller pattern and the more direct measurements of the charge state [29,31–34].

When the charge order is described in terms of integral charge states, they should be understood as oxidation states, which, per definition, attribute electrons as a whole to the more electronegative partner [35]. This is, however, a definition rather than a detailed description of an electron distribution. The notion of integral charge states Mn^{3+} and Mn^{4+} ions shall be understood in this context. The real charge distributions in manganites are more subtle.

IV. RESULTS AND DISCUSSION

A. Choice of the photon energy

The photoexcitation in manganites occurs through both d-to-d and p-to-d transitions in the spectral energy range ∼0.5–2.3 eV [16,36–39]. While the d-to-d transitions occur between Mn $3d$ states, the p-to-d transitions occur between O $2p$ and Mn d states [16,40,41]. The transitions observed experimentally in the ∼0.5–0.75 eV energy range are mainly dipole-allowed transitions from the occupied to the unoccupied e_g states. While d-d transition on a single Mn site are dipole forbidden, there are dipole-allowed transitions, which involve charge-transfer oscillations between different Mn sites [16]. In this work, we focus entirely on transitions within the Mn e_g shell. The charge-transfer transitions from O p to Mn d states dominate only at comparatively higher energies [16,36–39].

A quantity used to describe the excitation is the photon-absorption density D_p, which is the total number of photons absorbed per Mn site and pulse. We calculate it as

$$D_p := \frac{\Delta E^{\text{tot}}_{f-i}}{N_{\text{Mn}} \hbar\omega} \quad (23)$$

from the energy $\Delta E^{\text{tot}}_{f-i}$ added by the light pulse to the system with N_{Mn} Mn ions (see also Fig. 31). The division by the photon energy $\hbar\omega$ and N_{Mn} provides the number D_p of absorbed photons per Mn ion and pulse.

Another quantity, often used to characterize experiments, is the pump fluence F_p. It is the energy transmitted to the sample per pulse and unit area. The pump fluence determines together with the pulse duration the intensity of the light field.

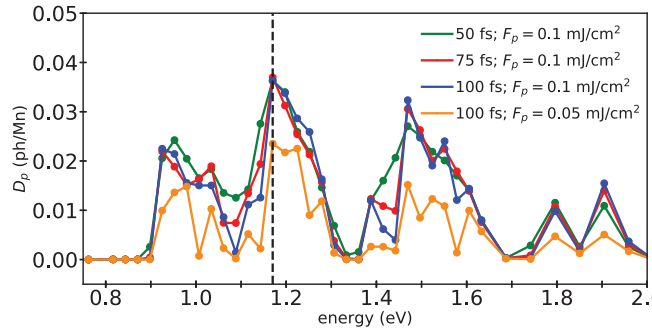

FIG. 4. Photon-absorption density D_p defined in Eq. (23) as function of the photon energy $E = \hbar\omega$ for different intensities and pulse lengths. The dashed line indicates the photon energy $\hbar\omega = 1.17$ eV chosen for the simulations described below.

The pump fluence F_p is

$$F_p = \frac{1}{2}|A_0|^2\omega^2 c\varepsilon_0 \int dt\, g(t)^2 = \frac{1}{2}|A_0|^2\omega^2 c\varepsilon_0, \quad (24)$$

where c is speed of light and ε_0 is vacuum permeability. With A_0 we denote the amplitude of the vector potential [see Eq. (7)]. The photon energy is $\hbar\omega$. Due to the normalization of the pulse-shape function $g(t)$ [Eq. (8)], the relation (24) is independent of the pulse duration. The spectral distribution of the photon-absorption density is shown in Fig. 4.

For the simulations discussed below, we have chosen the photon energy equal to the absorption maximum of $\hbar\omega = 1.17$ eV. The position of the absorption maximum appears to be rather independent of pulse length and light intensity.

Figure 5 shows the photon-absorption density D_p as a function of the amplitude A_0 of the light field, as defined in Eq. (7). At the largest fluences, every third electron is excited, which explains the large changes of the magnetic and polaronic microstructure observed in those simulations.

The photon-absorption density in Fig. 5 grows approximately linearly with the amplitude of the light field. This behavior differs from the low fluence regime, where the

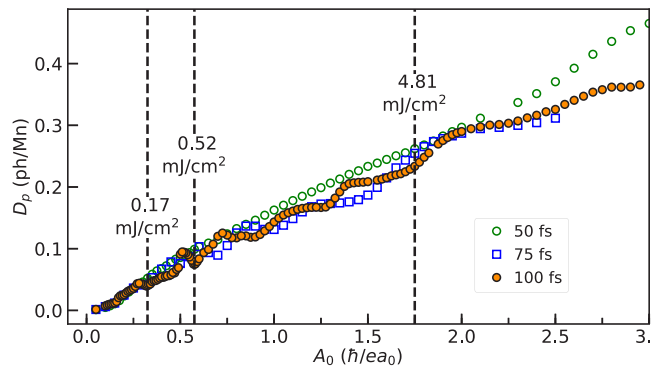

FIG. 5. Photon-absorption density D_p defined in Eq. (23) as function of the amplitude of the exciting field A_0 and a photon energy of $\hbar\omega = 1.17$ eV. Also given are the pump fluences F_p in units of mJ/cm^2 according to Eq. (24) for the boundaries of the four regimes discussed below in Sec. IV B.

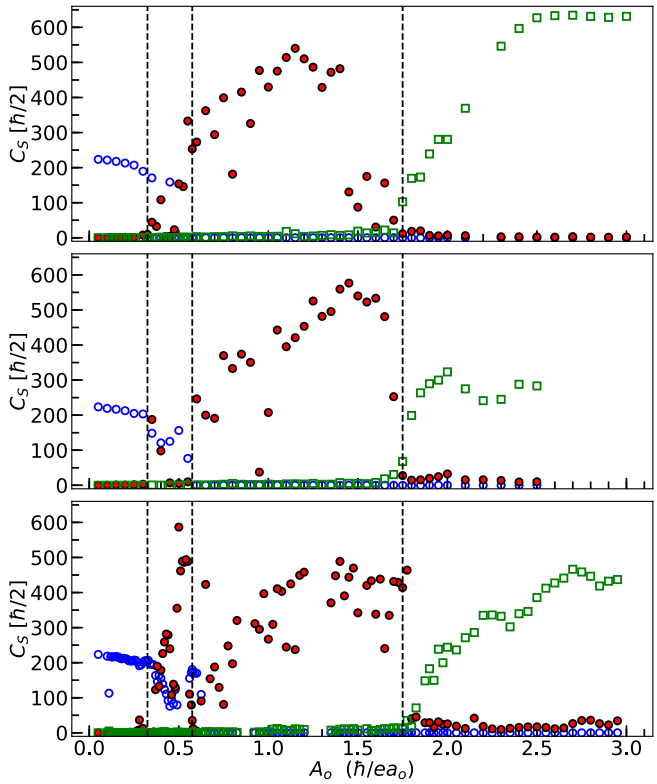

FIG. 6. Identification of the distinct regimes on the basis of the intensity of magnetic diffraction spots. The pulse lengths are 50, 75, and 100 fs from top to bottom. Open blue circles show the minimum values of the spin-correlation function $C_S(\frac{1}{2}, 1, 1)$ characteristic for the CE-type magnetic structure during the first 2 ps following the excitation. Red-filled circles are the maximum intensities $C_s(0, 0, 1)$ characteristic of the A-type magnetic structure and open green squares are maximum intensities $C_S(0, 1, 1)$ characteristic for the G-type structure.

photon absorption grows quadratically with the amplitude. The approximate linear behavior can be attributed to damping and decoherence. For a two-state system, the optical Bloch equations with damping have a steady-state solution with an excited-state population of $P_e(A_0) = A_0^2/(a + A_0^2)$, where a is constant determined, among others, by detuning and friction parameters [42]. P_e has a point of inflection at a population of 25%, which explains the approximate linear behavior on the amplitude for the fluences studied here. Additional features seen in Fig. 5 can be attributed in parts to strongly damped Rabi oscillations.

B. Regimes with distinct relaxation behavior

The relaxation following the optical absorption depends strongly on the pump fluence F_p. Based on the diffraction patterns, we identify four regimes with distinct relaxation behavior. The diffraction intensities of the characteristic diffraction spots are shown in Fig. 6. The boundaries of the different regimes depend little on the pulse duration.

The nature of these regimes is discussed in detail below. They can be characterized as follows:

TABLE III. Photon-absorption density D_p and fluence F_p for the A_0 values used in the graphs.

Regime	I	II	III	IV
$A_0(\hbar/(ea_0))$	0.20	0.45	0.53	2.50
D_p(ph/Mn)	0.025	0.058	0.094	0.326
F_p(mJ/cm^2)	0.063	0.32	0.44	9.81

(1) In regime I, the spin, charge, and orbital order is preserved. Coherent phonons with long lifetime are observed.

(2) In regime II, the spin dynamics sets in, but the spin pattern relaxes back to the original state on a picosecond timescale. The charge order remains unaffected. Coherent phonons are present as in regime I.

(3) In regime III and beyond, the charge order is disrupted and the system is driven into a photoinduced ferromagnetic state.

(4) In regime IV, the system enters a photoinduced antiferromagnetic state.

For the demonstration of the characteristic behavior in the four fluence regimes, we selected the fluence values in Table III.

The time-dependent distributions of excited electrons and holes are shown in Fig. 7. While the band structure for regimes I and II are qualitatively similar, in regime III the band gap at the Fermi level collapses as a ferromagnetic metallic state is formed. Also, the band gap between minority and majority spins collapses. The band gap between majority- and minority-spin orbitals reoccurs in regime IV, where the system evolves into a new antiferromagnetic state. The antiferromagnetism is accompanied by a smaller bandwidth of majority- and minority-spin bands so that the gap between them opens. Like in the ferromagnetic regime III, the system is metallic in regime IV.

C. Regime I

For the weak pump fluences of regime I, the magnetic, charge, and orbital orders remain intact. The excitation can be described as formation of electrons and holes in an essentially rigid band structure. The electron-hole pairs are strongly coupled to breathing modes and Jahn-Teller active phonons at the Γ point. As a consequence, two coherent phonons with a long lifetime are excited.

The excitation can be rationalized using the Wannier-type states introduced previously. They are shown in Fig. 1 for one segment of the zigzag chain. Unless mentioned otherwise, the electric field of the light wave points along the b direction of the *Pbnm* unit cell, that is, along to the zigzag chains of the ground-state magnetic structure.

1. During the light pulse

In the initial phase of the excitation, i.e., during the 100-fs light pulse, charge and orbital order drop to lower values. Furthermore, long-lived oscillations, discussed below, are initiated. On top of these effects, high-frequency oscillations of the electronic system are induced that, however, decay after few tenths of picoseconds. These oscillations are apparent in

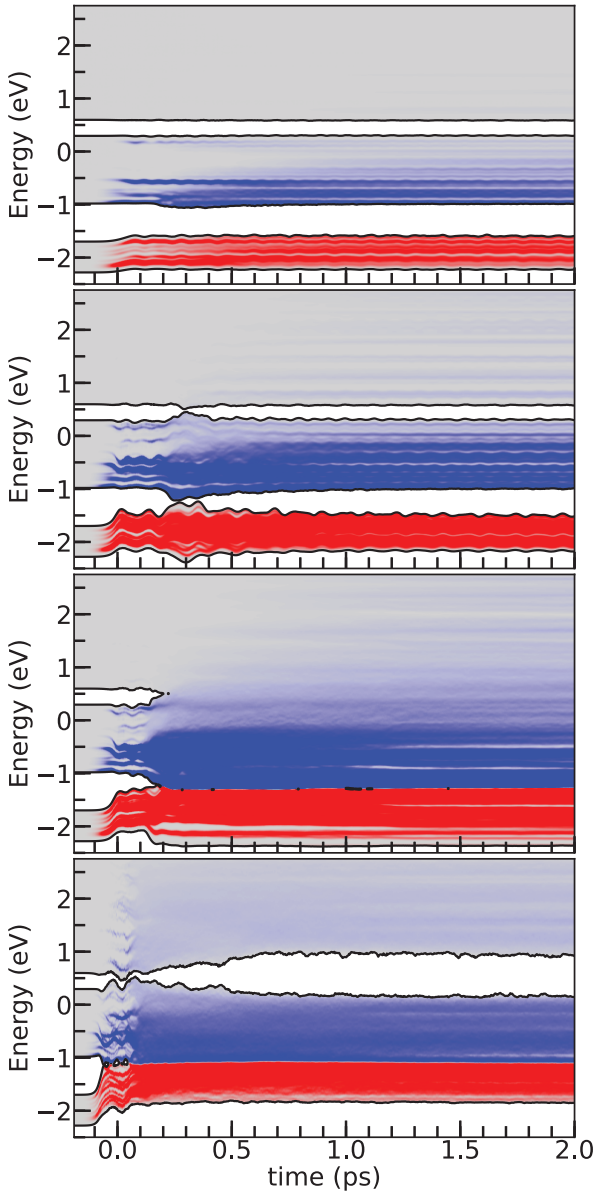

FIG. 7. Time evolution of the electron and hole distributions induced by a femtosecond pulse of different intensities. Regimes I to IV from top to bottom, i.e., $A_0 = 0.20, 0.45, 0.53, 2.50\ \hbar/(ea_0)$. The instantaneous one-particle spectrum of Born-Oppenheimer energies is shown in gray. The intensity of blue color indicates conduction electrons and that of red color indicates holes.

the charge-order and orbital-order diffraction peaks in Figs. 8 and 9.

The only dipole-allowed transitions are between the bonding orbital $|w_1\rangle$ and the nonbonding orbital $|w_2\rangle$ as well as between latter $|w_2\rangle$ and the antibonding orbital $|w_3\rangle$ with the same spin direction shown in Fig. 1. There are no dipole-allowed transitions to $|w_4\rangle$. Furthermore, there are no dipole-allowed transitions between Wannier-type orbitals from different segments of the zigzag chains.

There is only one type of dipole-allowed transition from the filled states. It lifts an electron from the majority-spin

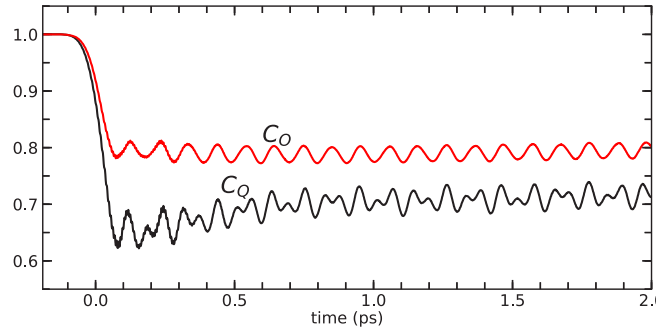

FIG. 8. Charge-order correlation $C_Q(1, 0, 0)$ (black) and orbital-order correlation $C_O(0, \frac{1}{2}, 0)$ (red) as function of time for regime I with $A_0 = 0.2\ \hbar/(ea_0)$. The correlations are scaled each so that their initial value is unity. The correlations can be represented well by a superposition of two harmonic oscillations with frequency $\nu_1 = 10$ THz and $\nu_2 = 16$ THz, which are the frequencies of the two coherent phonons.

bonding orbital $|w_1\rangle$ to the nonbonding orbital $|w_2\rangle$ of the same segment and with the same spin.

The nature of the high-frequency charge oscillation on a segment of the zigzag chain is rationalized via the Bloch waves of $|w_1\rangle$ and $|w_2\rangle$ character shown in Fig. 10, which are connected by the optical excitation. The excitation depends on the polarization of the light. Two representative Bloch waves of the initial state with $|w_1\rangle$ character and the corresponding final state with $|w_2\rangle$ character are shown schematically in Fig. 10 for each polarization in the *ab* plane. The product of initial- and final-state wave functions is proportional to the first-order change of the charge density, which is in turn

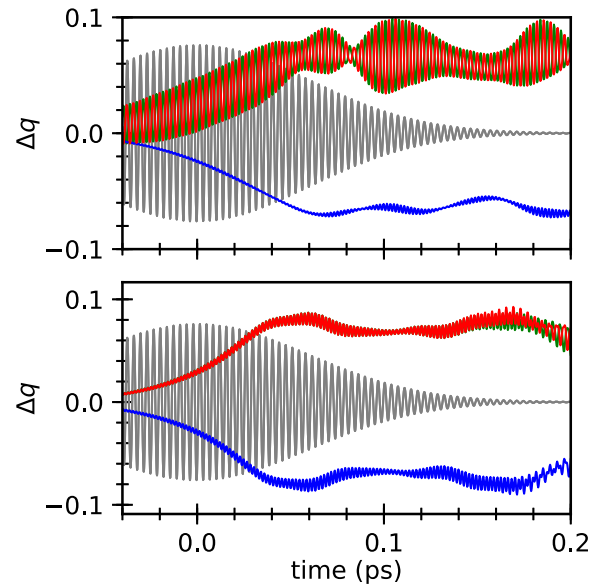

FIG. 9. Short-term dynamics for polarization along the *a* axis (top) and along the *b* axis (bottom) in regime I with $A_0 = 0.20\ \hbar/(ea_0)$. Shown are the deviations Δq of the charges from a trimer of the CE-type ground state as function of time: central site (blue) and corner sites (red/green). The instantaneous amplitude (arbitrary scale) of the light pulse is shown in gray.

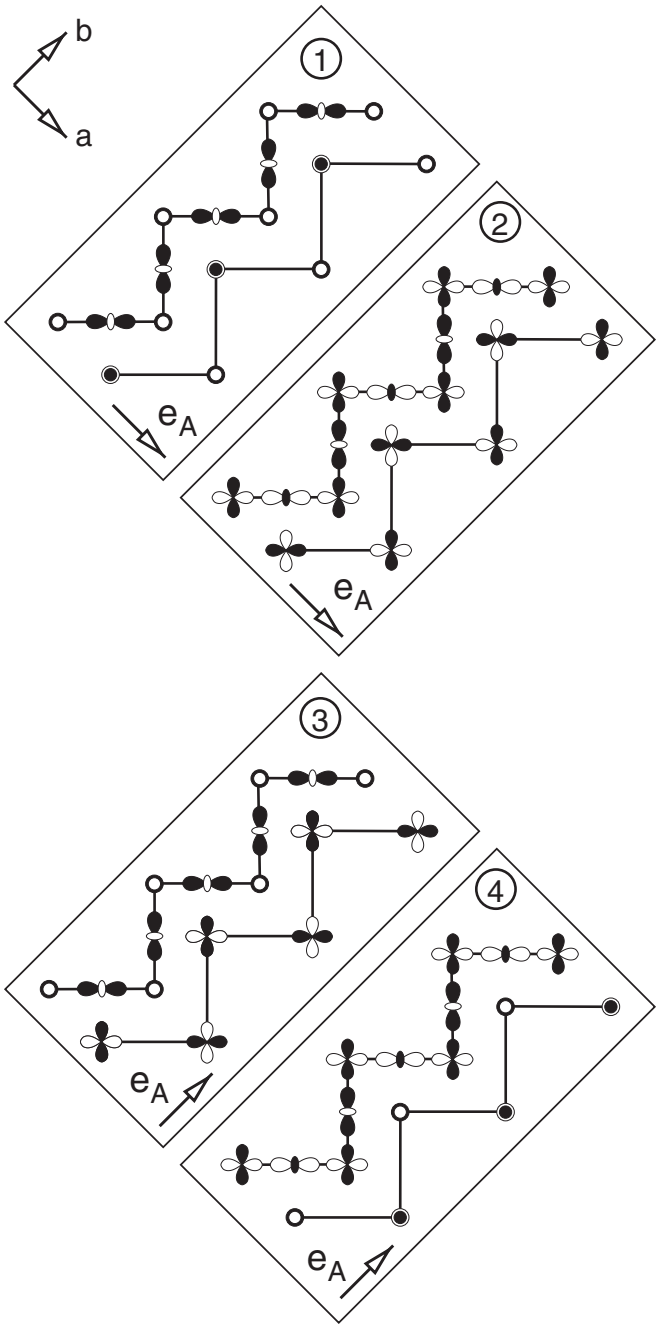

FIG. 10. Schematic drawing of Bloch waves involved in the photoexcitation with the electric field ($\vec{E} \parallel \vec{e}_A$) polarized perpendicular ($\vec{E} \parallel \vec{a}$) (1) and (2) or along ($\vec{E} \parallel \vec{b}$) (3) and (4) to the zigzag chains of the CE-type spin order. Each box shows the initial state with $|w_1\rangle$ character in the upper left and the final state with $|w_2\rangle$ character in the lower right. For each polarization, two pairs of initial and final states, one without and one with sign change from one segment to the other, are shown. The induced charge density is related in first order to the product of initial and final states.

responsible for the dipole oscillation that couples to the light field.

For an electric field along the a axis, i.e., perpendicular to the zigzag chains, large dipole oscillations between the two corner sites are visible in Fig. 9. The charges of the two corner sites (red/green in Fig. 9) oscillate out of phase and with the frequency of the light field. They describe the oscillating charge transfer between the corner sites. This is consistent with the Bloch waves (1) and (2) in Fig. 10 for $\vec{e}_A \parallel \vec{a}$. The product of initial, $|w_1\rangle$-derived, states and final, $|w_2\rangle$-derived, Bloch waves lead to charge contributions with alternating sign on the corner sites of a zigzag chain. The central site (blue in Fig. 9) has a smaller oscillation with twice the frequency of the light field. This oscillation is due to the rescaling of the $|w_1\rangle$ contribution required to maintain a normalized overall wave function, while $|w_2\rangle$ is mixed in.

When the electric field is polarized along the b axis, i.e., parallel to the zigzag chain, we observe in Fig. 9 only oscillations with small amplitude and with the doubled frequency of the light wave. The two corner sites oscillate in phase with the doubled frequency. The charges on the central sites oscillate out of phase with the corner sites. This is consistent with the Bloch waves (3) and (4) in Fig. 10: the product of $|w_1\rangle$- and $|w_2\rangle$-derived waves has contributions only on the corner sites. However, there, the product of two orthogonal orbitals is formed, which does not contribute to the net charge. The net charge dipole coupling to the light field is not apparent in the bulk. It would show up at the surface of the material. Thus, only the second-order charge oscillations describing the charge transfer from the central site to the corner sites are visible in the bulk. The charge oscillations between the corner sites are initially absent and only kick in at later times.

2. Orbital order

Let us now turn from the high-frequency electronic excitations during the light pulse to the changes that persist beyond the light pulse. For the analysis, we expand the time-dependent one-particle wave functions $|\psi_n(t)\rangle$ in Wannier-type orbitals

$$|\psi_n(t)\rangle = \sum_{j,\sigma,m} |w_{j,\sigma,m}\rangle\langle w_{j,\sigma,m}|\psi_n(t)\rangle. \tag{25}$$

The Wannier-type orbitals $|w_{j,\sigma,m}\rangle$ have spin σ ($\sigma \in \{\uparrow, \downarrow\}$) and belong to the trimer m of the unit cell. Index j ($j \in 1, 2, 3, 4$) selects one of the four Wannier states from a given trimer according to Fig. 1.

The instantaneous occupancy $F_j^{\mathrm{tot}}(t)$ of the jth Wannier-type state $|w_j\rangle$ is

$$F_j^{\mathrm{tot}} = \frac{2}{N_{\mathrm{Mn}}} \sum_m \sum_\sigma Q_{j,m,\sigma,\sigma} \tag{26}$$

and its spin polarization is

$$F_j^{\mathrm{spin}} = \frac{2}{N_{\mathrm{Mn}}} \times \sum_m \sqrt{(Q_{j,m,\uparrow,\uparrow} - Q_{j,m,\downarrow,\downarrow})^2 + 4Q_{j,m,\uparrow,\downarrow}Q_{j,m,\downarrow,\uparrow}} \tag{27}$$

with the number of Mn sites N_{Mn} and

$$Q_{j,m,\sigma,\sigma'} = \sum_n \langle w_{j,\sigma,m}|\psi_n\rangle f_n \langle \psi_n|w_{j,\sigma',m}\rangle. \tag{28}$$

As shown in Fig. 11, the dipole-allowed optical transitions from $|w_1\rangle$ to $|w_2\rangle$ dominate at the low pump fluences of

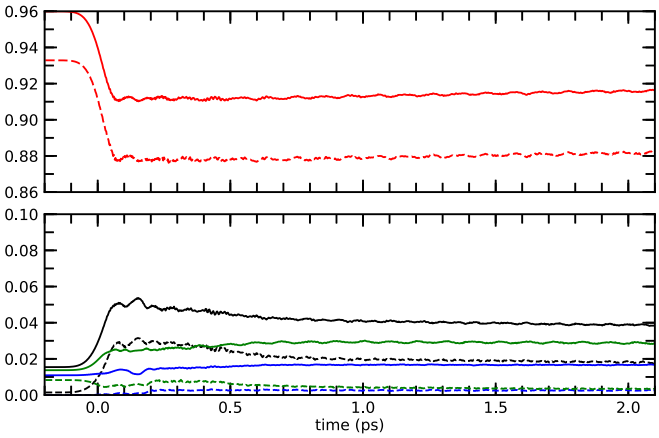

FIG. 11. Total occupancies $F_j^{\mathrm{tot}}(t)$ (full lines) of Wannier-type orbitals $|w_j\rangle$ and their spin polarization $F_j^{\mathrm{spin}}(t)$ (dashed lines) as function of time for fluence regime I with $A_0 = 0.20\ \hbar/(ea_0)$. Occupancies of $|w_1\rangle$ (red), $|w_2\rangle$ (black), $|w_3\rangle$ (blue), and $|w_4\rangle$ (green).

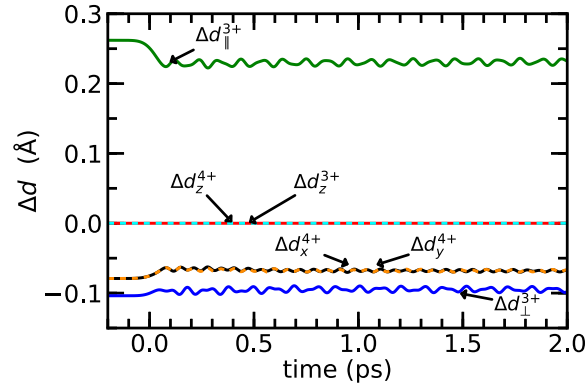

FIG. 12. Phonon modes of region I with $A_0 = 0.20\ \hbar/(ea_0)$. Shown are the expansions Δd of the oxygen distances along the octahedral axes. The superscript 3+ refers to the formal charge state of the central Mn ion in a trimer of the zigzag chain of the CE-type magnetic structure, while 4+ refers to the corner site. For the central octahedron, the expansion along the trimer axis is $\Delta d_{\parallel}^{3+}$ and the expansion in the *ab* plane perpendicular to the trimer axis is $\Delta d_{\perp}^{3+}$. The planar displacements at the corner atoms along and in the *ab* plane perpendicular to the trimer axis Δd_x^{4+} and Δd_y^{4+} are identical. The expansions in the *c* direction, indicated by a subscript *z*, vanish. Visible is the initial reduction of the Jahn-Teller distortion, followed by the coherent breathing mode with 16 THz on the corner sites and a Jahn-Teller mode at the central site with 10 THz. The displacements are averaged over equivalent atoms.

regime I. Thus, the occupancy of $|w_2\rangle$ grows at the expense of $|w_1\rangle$ during the light pulse, while the occupancies of $|w_3\rangle$ and $|w_4\rangle$ remain small. After the light pulse, the occupation of $|w_2\rangle$ remains almost constant, which is one sign of the preservation of the ordered state of the material.

Often, e.g. [43], the excitation is attributed to an onsite *d*-to-*d* transition at the central Mn site of a trimer segment, which formally is the Mn^{3+} ion. The picture, which emerges from our calculations, is more subtle. Rather than a dipole-forbidden excitation on central Mn ion from $|w_1\rangle$ to $|w_4\rangle$, the excitation is a $|w_1\rangle$-to-$|w_2\rangle$ charge-transfer excitation, which displaces electrons from the central Mn ions to the corner Mn ions. This transition does not exist in the limit of complete charge order. The description in terms of Wannier-type orbitals in Fig. 1 explains the strong optical absorption and it has consequences on the coherent modes described below.

3. Charge order

The $|w_1\rangle$-to-$|w_2\rangle$ repopulation rearranges electrons from the central to the corner sites, which reduces the charge disproportionation between central and corner sites. The reduced charge disproportionation reflects on the charge-order correlation $C_Q(0, 1, 0)$ shown in Fig. 8. The light pulse induces a sharp drop of the charge-order diffraction intensity $C_Q(1, 0, 0)$ from the initial value. Then, the intensity oscillates around this reduced intensity, with little sign of recovery during our simulation.

In our simulation, the orbital-order peak $C_O(0, \frac{1}{2}, 1)$ has a characteristic frequency of 10 THz, while the charge-order diffraction peak $C_Q(1, 0, 0)$ exhibits one frequency at 10 THz and a second one at 16 THz.

4. Coherent vibrations

The removal of electrons from the central site during the $|w_1\rangle$-to-$|w_2\rangle$ transition reduces its Jahn-Teller distortion. The sudden change excites a Jahn-Teller mode with $\nu = 10$ THz, which affects predominantly the central site. The displacements as function of time are shown in Fig. 12.

The charge transfer from central to the corner sites reduces the charge order and thus induces a planar breathing mode on the corner sites with a frequency of $\nu = 16$ THz. Note, that an electron addition to a Mn site populates the Mn-O antibonds, which, in turn, expands the nearest-neighbor distances. The expansion of the corner sites also affects the Jahn-Teller vibration on the central site.

On the timescale of a few picoseconds, the vibrations do not dissipate significantly. Furthermore, the phonon modes are fully coherent on the picosecond timescale of our calculation. We attribute the lack of dissipation to the absence of heat conduction. In an experiment, a limited spot is illuminated and the energy can escape from the illuminated region by heat conduction. In our simulation, this process is prohibited because the infinite material is illuminated homogeneously.

Another reason for an unexpectedly slow dissipation is the specific nonequilibrium state at hand. The coherent phonons are in contact with a phonon bath that is extremely cold. Thus, the collision probability of the coherent phonon with another one is extremely small.

Pump-probe reflectivity measurements [44] of $Nd_{1/2}Ca_{1/2}MnO_3$, another manganite with the CE-type ground state, provided frequencies with 2.5 THz (82 cm^{-1}), 6.7 THz (224 cm^{-1}), 10.2 THz (339 cm^{-1}), and 14.1 THz (469 cm^{-1}). A coherent vibration with 14 THz has been experimentally observed also for $La_{1/2}Ca_{1/2}MnO_3$ [45] and $Pr_{1/2}Ca_{1/2}MnO_3$ [43,46] for a weak photoexcitation, i.e., below a photoabsorption density of $D_p < 0.01$, and attributed to Jahn-Teller modes.

The two highest frequencies measured in $Nd_{1/2}Ca_{1/2}MnO_3$ [44] at 10.2 and 14.1 THz agree very well with those in

our simulations. This suggests a different assignment of the coherent vibrational modes: the mode previously assigned to a octahedral rotation mode at 10 THz is in our simulation a Jahn-Teller oscillation on the central site of a segment. The mode assigned as Jahn-Teller mode at 16 THz is in our simulation a symmetric breathing mode at the corner sites. Overlapping with the 10-THz vibration, we also find the antisymmetric expansion of the corner sites along the trimer axis. This latter vibration, however, is not coupled to the optical excitation. It should be noted that displacements of the oxygen ions in our model, denoted as the Jahn-Teller and breathing modes, also have a small implicit component from octahedral tilting.

Vibrations observed in the low-frequency range 2.4–7 THz [7,43–46] have been attributed to A-type ion motion and rotational modes of MnO_6 octahedra. Our model does not describe these low-frequency modes because it does not contain explicit A-type ions. Pure octahedral rotations are not included because our model does not describe oxygen vibrations perpendicular to the oxygen bridge.

Our description of the coherent phonons differs from that given earlier [44] as being due to an instantaneous melting of the charge and orbital order. The picture emerging from our simulations is that of a mechanistic rather than a thermal process.

5. Magnetic order

In the fluence regime I, the magnetic order is preserved: The spin angles deviate by about 10° from the ideal ground-state arrangement.

D. Regime II: Transient changes of the magnetic order

In the fluence regime II, the Jahn-Teller-active phonons respond similar to regime I. After an initial period of about 200 fs, however, also the spin order is perturbed. The spin system relaxes back into the ground state within a few picoseconds, while the reduction of charge and orbital order persists much longer.

1. Magnetic order

As shown in Fig. 13, the spin correlations of the initial CE-type order drop to lower values at about 0.2 ps, while a prominent but short-lived signal of an A-type magnetic order shows up. This signal lives for about 0.2 ps before it dies out again. The spin-diffraction pattern during this period, which reflects the superposition of CE-type and A-type spin patterns, is shown in the left graph of Fig. 14.

As shown in Fig. 15, the angle of antiferromagnetic neighbors changes by up to 90°. Aside from some fluctuations, the ferromagnetic order within the zigzag chain is preserved in the fluence regime II. What is affected most is the spin correlation between neighboring chains in the *ab* plane. The onset time decreases with increasing fluence.

We attribute the response of the spin system to the optically induced intersite spin transfer (OISTR) [47] caused by the coupling of the majority-spin $|w_2\rangle$ states with minority-spin states $|w_1\rangle$ and $|w_4\rangle$ of a neighboring zigzag chain: the time-dependent populations of the relevant Wannier-type orbitals

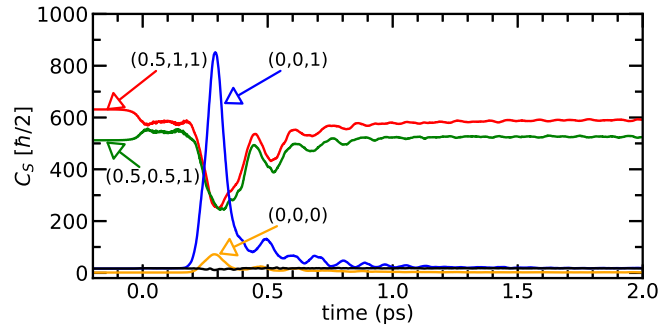

FIG. 13. Spin-correlation function of regime II with $A_0 = 0.45\ \hbar/(ea_0)$. The correlation functions $C_S(\frac{1}{2}, 1, 1)$ and $C_S(\frac{1}{2}, \frac{1}{2}, 1)$ are characteristic for the CE-type ground state. The correlation function $C_S(0, 0, 1)$ is characteristic for A-type magnetic structure. The ferromagnetic (B-type) peak $C_S(0, 0, 0)$ is shown in orange. The CE-type structure recovers after a transient period.

are shown in Fig. 16. The $|w_2\rangle$ state is populated by the photoexcitation. It is located at the corner sites and has lobes pointing toward the central atom of a neighboring zigzag chain. Thus, there is a spatial overlap of the $|w_2\rangle$ orbitals with the minority-spin $|w_1\rangle$ and $|w_4\rangle$ orbitals of a neighboring chain. The excitation into the $|w_2\rangle$ orbital is therefore accompanied by a spin transfer between neighboring zigzag chains in the *ab* plane. The delocalization of electrons among the antiferromagnetically coupled zigzag chains changes the magnetization of the e_g electrons, which in turn acts onto the classical spins describing the t_{2g} electrons and which causes transient or permanent changes of the magnetization pattern.

In the period from 0.2 to 0.4 ps in Fig. 16, we observe a transfer of weight from $|w_1\rangle$ orbitals of one chain to the majority spin $|w_4\rangle$ of a neighboring chain. This is a consequence of the transient magnetic transition, which takes place during this period. The hybridization between these orbitals becomes possible because the spin orientation of neighboring chains deviates from 180°.

In order to obtain a better understanding of these spin fluctuations, we investigated the spin structure as function of the ratio of excited electrons. For this purpose, we reduce the occupation for the $\frac{1}{2}N_{\mathrm{Mn}}$ occupied states from 1 to $1 - \delta$ and we increase the occupation of the first $\frac{1}{2}N_{\mathrm{Mn}}$ unoccupied states

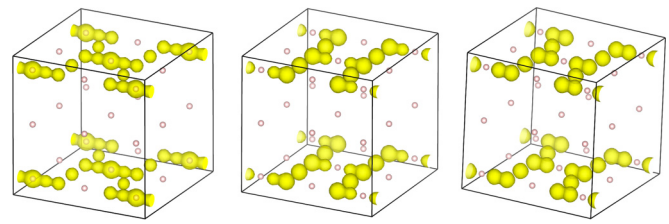

FIG. 14. Spin-diffraction patterns in regime II with $A_0 = 0.45\ \hbar/(ea_0)$. At about 0.29 ps (left), the magnetic structure is a superposition of patterns of the CE-type and the A-type antiferromagnetic structures. At 0.5 ps (middle), a spin wave emerges, which is similar to obtained in equilibrium with $\delta = 15\%$ excited electrons (right).

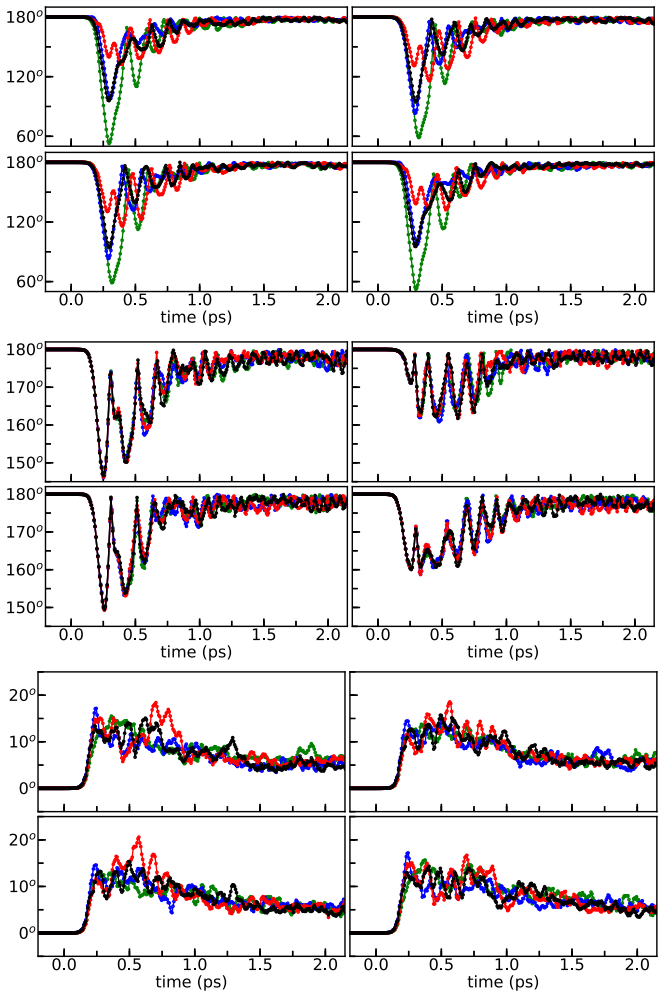

FIG. 15. Spin correlations in regime II with $A_0 = 0.45\ \hbar/(ea_0)$ as function of time. $\Phi_{n,n'}$ is the angle between the spins $\langle\vec{S}\rangle_n$ of neighboring zigzag chains C_n and $C_{n'}$. The mean angle of a chain is $\langle\vec{S}\rangle_n = \frac{1}{N}\sum_{j\in C_n}\vec{S}_j$, where N is the number of Mn sites in the chain. The top four figures show the angles $\Phi_{n,n'}$ for neighboring chains in the same *ab* plane. The middle four figures show the angles for neighboring chains stacked along the *c* direction. The bottom four figures show the ferromagnetic spin correlations within a chain $\Delta_n = \sqrt{\frac{1}{N}\sum_{j\in C_n}[\angle(\vec{S}_j, \langle\vec{S}\rangle_n)]^2}$.

from 0 to δ. Then, we investigate the ground state as function of δ, where all degrees of freedom except strain are relaxed.

The original CE-type spin order is preserved up to $\delta = 11\%$. For larger δ, a noncollinear but coplanar spin-wave structure emerges, where every two antiferromagnetic zigzag chains in the *ab* plane pair up and form a finite spin angle with the spin axis of the next pair. The ferromagnetic spin order within the zigzag chains and the strict antiferromagnetic coupling in the *c* direction remain intact. The angle of the spin axes grows with increasing δ until the angle approaches 90°. At this point, $\delta \approx 16\%$, the system collapses into a ferromagnetic metallic state.

Hence, we interpret the spin fluctuation observed in the simulations as the onset of a Néel transition, which, in this case, is driven by photoexcited rather than by thermal $|w_1\rangle \rightarrow$

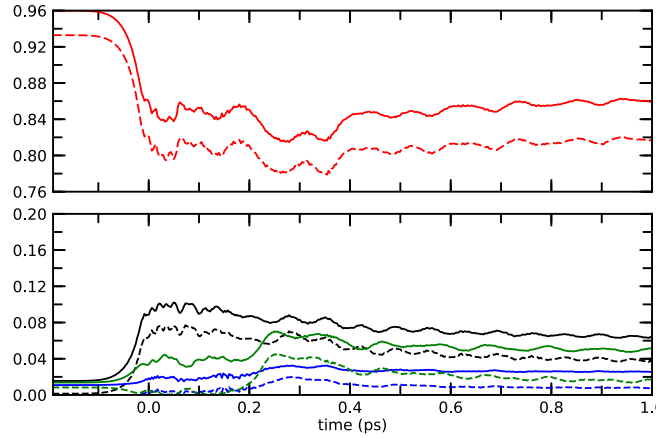

FIG. 16. Total occupancies $F_j^{\rm tot}(t)$ (full lines) of Wannier-type orbitals $|w_j\rangle$ and their spin polarization $F_j^{\rm spin}(t)$ (dashed lines) as function of time for fluence regime II with $A_0 = 0.45\ \hbar/(ea_0)$. Occupancies of $|w_1\rangle$ (red), $|w_2\rangle$ (black), $|w_3\rangle$ (blue), and $|w_4\rangle$ (green).

$|w_2\rangle$ electron-hole pairs. In this context, the OISTR concept may be generalized to a temperature-induced intersite spin transfer (TISTR).

2. Charge order

Charge and orbital order, Fig. 17, as well as coherent phonons, Fig. 18, show the same behavior as in regime I, albeit with larger amplitude. The oscillations of the phonon displacements and the correlation functions for charge and orbital order are long lived. Unlike regime I, a slow decay of the oscillations is noticeable in regime II.

The coherent phonons, charge order, and orbital order are only little affected by the transient change of the magnetic structure. The reason is that the charge order and orbital order remain intact during the transient change of the magnetic correlations.

Coherent phonons, charge order, and orbital order are strongly coupled via electron-phonon coupling. They are due to the same physical mechanism, namely, the $|w_1\rangle$ to $|w_2\rangle$ excitation. Thus, they are expected to exhibit similar decay properties.

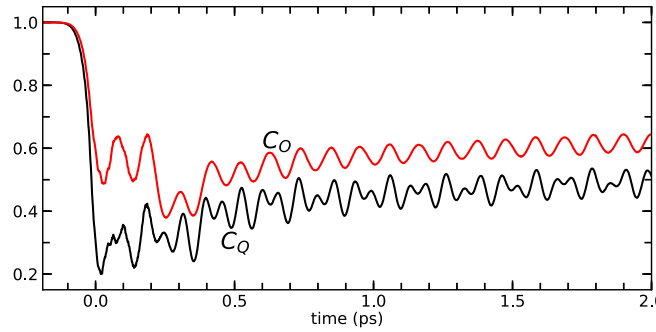

FIG. 17. Charge-order correlation $C_Q(1,0,0)$ (black) and orbital-order correlation $C_O(0,\frac{1}{2},0)$ (red) as function of time for regime II with $A_0 = 0.45\ \hbar/(ea_0)$. The correlations are scaled each so that their initial value is unity.

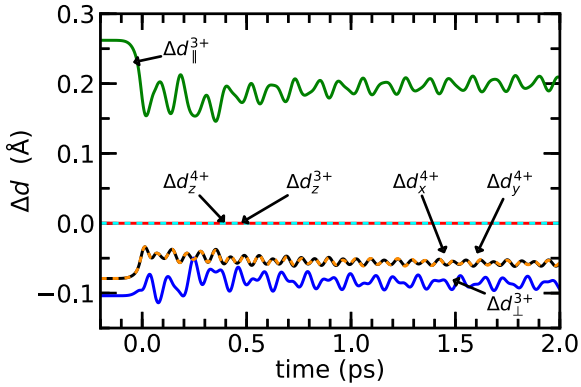

FIG. 18. Phonon modes of regime II with $A_0 = 0.45\ \hbar/(ea_0)$. For a description of the symbols, see Fig. 12.

E. Regime III: Photoinduced ferromagnetism

In regime III, the system undergoes a photoinduced phase transition, which converts the CE-antiferromagnetic order into a ferromagnetic metallic state without charge and orbital order.

1. Magnetic order

Initially, the antiferromagnetic correlation between the zigzag chains is perturbed rather similar to regime II, leading to an A-type magnetization as seen in Fig. 19. Unlike regime II, however, the A-type diffraction pattern persists for several picoseconds. During this time, the diffraction pattern of the ferromagnet builds up until it replaces the A-type diffraction pattern altogether.

The ferromagnetic state obtained is not fully established in the simulation: the nonrelativistic Schrödinger equation employed in the simulations conserves the total spin. As a result, the system evolves into a state that is better characterized as a spin wave or a lattice of ferromagnetic domains.

Nevertheless, the diffraction pattern obtained is very similar to the ferromagnetic structure. For each diffraction spot

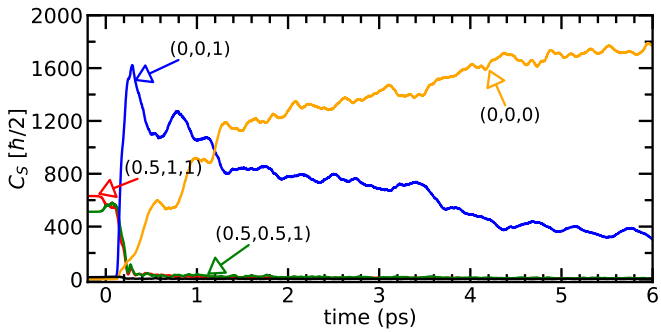

FIG. 19. Spin-diffraction intensity of regime III with $A_0 = 0.53\ \hbar/(ea_0)$. The peaks $C_S(0.5, 1, 1)$ and $C_S(0.5, 0.5, 1)$ shown in red, respectively green, are characteristic for the CE-type ground state. The peak $C_S(0, 0, 1)$ shown in blue is characteristic for A-type magnetic structure. The ferromagnetic (B-type) peak $C_S(0, 0, 0)$ is shown in orange. The original CE-type magnetic pattern is quickly destroyed, while an A-type magnetic pattern emerges. The latter evolves over time into a the ferromagnetic phase.

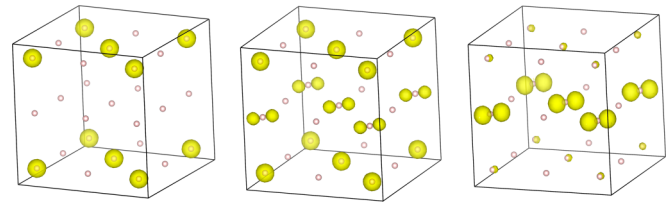

FIG. 20. Magnetic diffraction patterns of region III with $A_0 = 0.53\ \hbar/(ea_0)$ at 0.3, 1.2, and 6.1 ps. The a axis points right, the b-axis toward the back, and the c axis up. The small white spheres indicate points with integer h, k, l in the *Pbnm* setting. Reciprocal space is shown for $h, k, l \in [-1.25, 1.25]$. At 0.3 ps the diffraction pattern is dominated by an A-type pattern. At 1.2 ps the diffraction pattern exhibits spots from both A and B types, while at 6.1 ps the diffraction pattern is ferromagnetic, i.e., B type. The double spots are a sign of ferromagnetic magnetic domains, respectively a long-wavelength spin wave, rather than a pure ferromagnet.

of the ferromagnetic structure, we do not obtain a single spot, but a set of two "twin peaks." The two peaks are located at the supercell reciprocal-space vectors adjacent to those of the ideal ferromagnet as seen in Fig. 20. The displacement of the twin peaks from the diffraction spot of a true ferromagnet is governed by the size of our supercell, which limits the wavelength of the spin wave, respectively the domain size.

The ferromagnetic spin correlation function in Fig. 19 exhibits a finite signal by considering the contribution from the immediate neighborhood of the specified reciprocal-lattice vector. The signal at the center of the spot is zero. We envisage that a larger supercell leads to larger domains and thus to twin peaks that are even closer together, making them indistinguishable by experiment.

2. Charge order

As shown in Fig. 21, the charge-order correlation C_Q and the orbital-order correlation C_O are completely wiped out after about 0.2 ps. The loss of orbital order makes the system metallic as seen in Fig. 7. The loss in charge and orbital order is also reflected in attenuation of the phonon displacements shown in Fig. 22.

We attribute the ferromagnetic order to a mechanism in the spirit of the double-exchange picture [48–50]. The origin

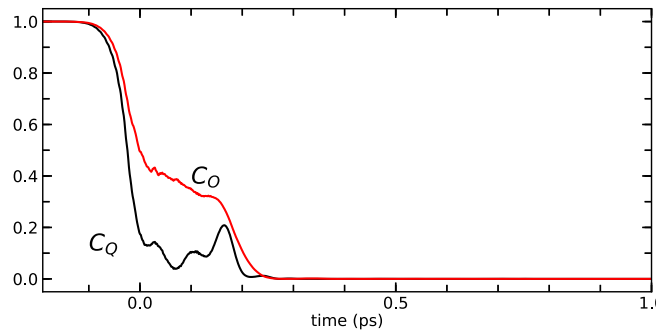

FIG. 21. Charge-order correlation $C_Q(1, 0, 0)$ (black) and orbital-order correlation $C_O(0, \frac{1}{2}, 0)$ (red) as function of time for regime III with $A_0 = 0.53\ \hbar/(ea_0)$. The correlations are scaled each so that their initial value is unity.

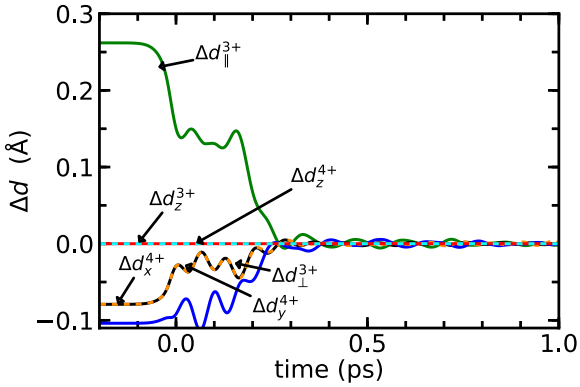

FIG. 22. Phonon modes of region III with $A_0 = 0.53\ \hbar/(ea_0)$. For a description of the symbols, see Fig. 12.

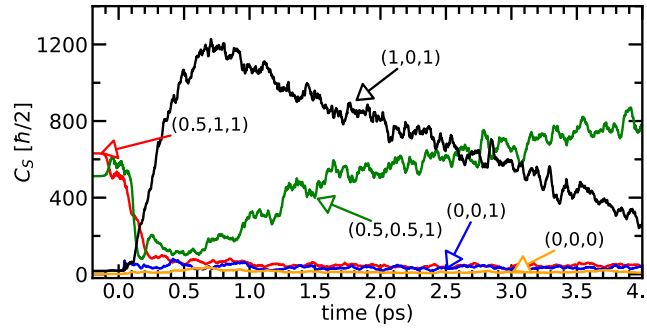

FIG. 23. Spin-diffraction intensity of regime IV with $A_0 = 2.50\ \hbar/(ea_0)$. The peaks $hkl = (0.5, 1, 1)$ and $(0.5, 0.5, 1)$ shown in red, respectively green, are characteristic for the CE-type ground state. The ferromagnetic (B-type) peak $C_S(0, 0, 0)$ is shown in orange. The peak with $hkl = (1, 0, 1)$ is characteristic for G-type magnetic structure. Over time, a new, noncollinear magnetic structure (see Fig. 25) emerges evidenced by the occurrence of the peak $hkl = (0.5, 0.5, 1)$.

of the band gap in the ground state of $Pr_{1/2}Ca_{1/2}MnO_3$ is the formation of Zener polarons. These Zener polarons are also the origin of charge and orbital order. Due to the repopulation of electrons across the band gap, the stabilization due to Zener polarons is lost and another, competing, mechanism can take over. A ferromagnetic alignment of the spins lowers the kinetic energy of the electrons, which can now spread over a large area: an electron with a given spin is effectively excluded from orbitals of Mn ions with opposite spin. A Mn ion with opposite spin thus leads to an energy cost. Thus, it is favorable, when all spins align ferromagnetically. In other words, a configuration of ferromagnetic spins produces a larger effective bandwidth of the majority-spin configuration. The larger bandwidth stabilizes electrons which populate the lower half of the majority-spin band formed.

3. Experiment

A recent ultrafast pump-probe experiment [46] carried out on $Pr_xCa_{1-x}MnO_3$ at 100 K with different pump fluences showed that the characteristic charge- and orbital-order reflection peaks of the CE-type ground state disappear for larger fluences $F_p > 2.5\ \mathrm{mJ/cm^2}$.

The experimental study with the same material class by Li *et al.* [51] revealed a photoinduced ferromagnetic state within about 120 fs above the threshold fluence $F_p = 2.4\ \mathrm{mJ/cm^2}$. A rise in magnetization has also been measured by Zhou *et al.* [52].

The measured threshold fluence of $F_p = 2.5\ \mathrm{mJ/cm^2}$ translates via Eq. (24) into an amplitude $A_0 = 1.26\,\hbar/(ea_0)$. In our simulations, the loss of charge and orbital order sets in with $A_0 = 0.58\,\hbar/(ea_0)$ ($F_p = 0.52\ \mathrm{mJ/cm^2}$) as seen in Fig. 6 from the appearance of the A-type magnetic order, which finally converts into the B-type (ferromagnetic) order. Our simulations and experiments produce the transition in the same fluence range. The remaining difference of a factor 5 in the threshold fluence may be attributed, for example, to the different photon energies.

It is worth mentioning that the ferromagnetic states observed in our study for region III is expected to persist on longer timescale hinting toward its possible long lifetime. Similar long-lived states are recently observed in $Pr_xCa_{1-x}MnO_3$ series within the charge-ordered region of the phase diagram [7].

F. Regime IV: Noncollinear antiferromagnet

In regime IV with the highest fluence, the system evolves first into a G-type antiferromagnet as shown in Fig. 23, rather than forming an A-type antiferromagnet as in regime III. After about 1.5 ps, the diffraction spots of the G-type structure fall off again in favor of a more complicated structure with noncollinear magnetic order. We note that this regime may be difficult to access experimentally due to the limited stability of the material.

The diffraction patterns calculated for characteristic times along the trajectory are shown in Fig. 24. The spin structure of the final state, which emerges at approximately 1.5 ps after the light pulse has been extracted on the basis of the real-space spin-correlation function. It is shown in its idealized form in Fig. 25. All spins are perpendicular to its neighbors in the *ab* plane and antiferromagnetic in the *c* direction. This model produces the spin diffraction pattern of the final spin configuration of regime IV. To our knowledge, this

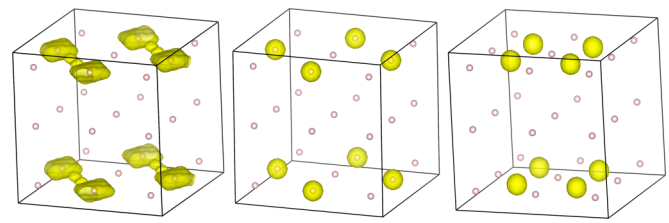

FIG. 24. Magnetic diffraction patterns of region IV with $A_0 = 2.50\ \hbar/(ea_0)$ at 0.3, 0.8, and 6.2 ps. At 0.3 and 0.8 ps the diffraction pattern is dominated by a G-type pattern. At 6.2 ps a new diffraction pattern occurs, which can be attributed to a noncollinear spin structure described in the text and in Fig. 25. Reciprocal space is shown for $h, k, l \in [-1.25, 1.25]$. The *a* axis points right, the *b* axis toward the back, and the *c* axis up. The small spheres indicate points with integer *hkl* in the *Pbnm* setting.

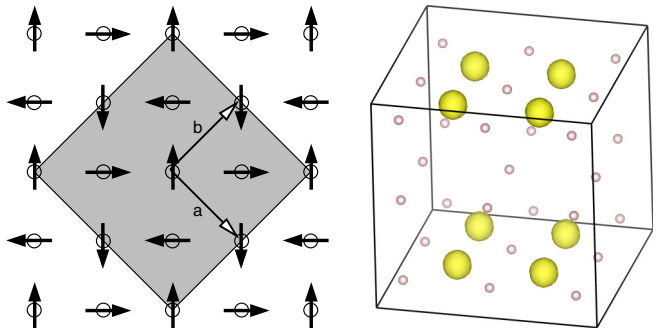

FIG. 25. Idealized model for the spin distribution reached in regime IV beyond 2 ps. The noncollinear spin structure in the *ab* plane of the *Pbnm* setting is shown on the left. Shown is the grid of Mn sites with the orientation of the t_{2g} spins. Planes are stacked antiferromagnetically in the *c* direction. On the right, the corresponding magnetic diffraction pattern is shown. The diffraction pattern is nearly indistinguishable from the one shown in Fig. 24, which is obtained in regime IV at 6.2 ps after the light pulse. The *a* axis points right, the *b* axis toward the back, and the *c* axis up. The small spheres indicate points with integer *hkl* in the *Pbnm* setting. Reciprocal space is shown for $h, k, l \in [-1.25, 1.25]$.

configuration has not been investigated before in the context of manganites.

The charge and orbital orders are destroyed almost immediately, that is, during the light pulse as shown in Fig. 26. This destruction of the orbital order excites phonons, that, however, dissipate on a picosecond timescale as seen in Fig. 27. The amplitude of the phonon vibrations is considerably larger than that in regime III.

We attribute the transition with increasing fluence from a ferromagnet in regime III to the noncollinear antiferromagnetic structure in regime IV to a mechanism analogous to that described earlier [53]. The double-exchange mechanism favors ferromagnetism through the increase in bandwidth only, when a majority of electrons populate the lower half of the majority-spin e_g states. Thus, increasing the fluence beyond a certain point switches off the double-exchange mechanism again, so that an antiferromagnetic structure can develop. The reduction of the bandwidth of majority-spin and minority-spin electrons opens a band gap between them, which is seen in

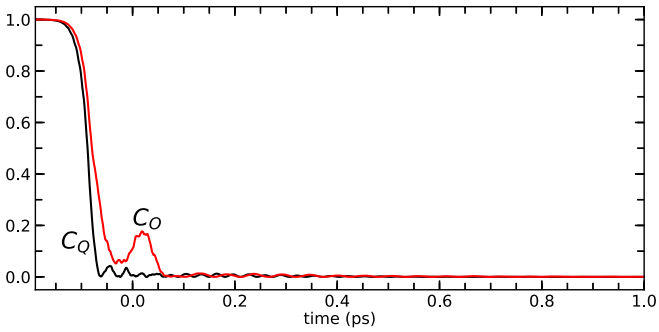

FIG. 26. Charge-order correlation $C_Q(1, 0, 0)$ (black) and orbital-order correlation $C_O(0, \frac{1}{2}, 0)$ (red) as function of time for regime IV with $A_0 = 2.5\ \hbar/(ea_0)$. The correlations are scaled each so that their initial value is unity.

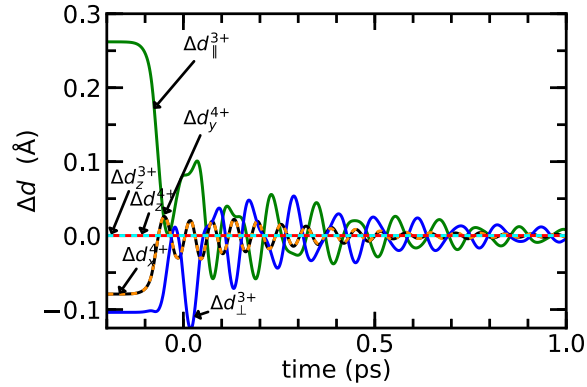

FIG. 27. Phonon modes of region IV with $A_0 = 2.50\ \hbar/(ea_0)$. For a description of the symbols, see Fig. 12.

Fig. 7. Compared to the minimal model [53], our system evolves into a more complicated noncollinear antiferromagnetic structure.

G. Thermalization

One of the questions of interest is how thermal equilibrium is established from the excited state. Therefore, we investigated the evolution of the temperatures of the subsystems.

Below, we consider the quasitemperatures described in Appendix D 1. As shown in Fig. 28, the light pulse immediately raises the temperature of the electronic system to high temperatures, i.e., several thousands of Kelvin, while the temperatures of the phonon and spin systems remain low in comparison. Thus, a state far from equilibrium is formed. The state is analogous to that of a nonthermal (cold) plasma, where the electrons reach 10^4 K, while the ions remain near room temperature.

While the temperature of the phonon system remains cold, the coherent phonons of regimes I and II are strongly coupled to the electronic subsystem and reach comparable temperatures. When we attribute the complete thermal energy of the ions considered to the two phonon modes, the resulting temperature of the two modes is comparable to the electronic temperature.

1. Nonequilibrium distribution of the electrons

In particular, the channel of the electrons is of interest because the energy from this channel is most easily put into practical use, such as in a solar cell. Our simulations may shed light onto the workings of the Boltzmann equation. For this purpose, we inspect the emergence of a distribution, i.e., the occupations, as function of energy and we compare the distribution obtained in our calculation with the Fermi distribution. The approach to a Fermi distribution is one of the common assumptions made for the Boltzmann equation.

In order to explore the approach to the Fermi distribution, we choose a representation of $\operatorname{atanh}(1 - 2\bar{f}_j)$ versus energy ϵ_j^{BO}. In this representation, a Fermi distribution maps onto a straight line with slope $1/k_B T_\psi$ and zero μ_ψ.

The Born-Oppenheimer energies ϵ_j^{BO}, their occupations $\bar{f}_j$, and the Born-Oppenheimer wave functions $|\phi_j^{\mathrm{BO}}\rangle$ are defined in Appendix D 1 b.

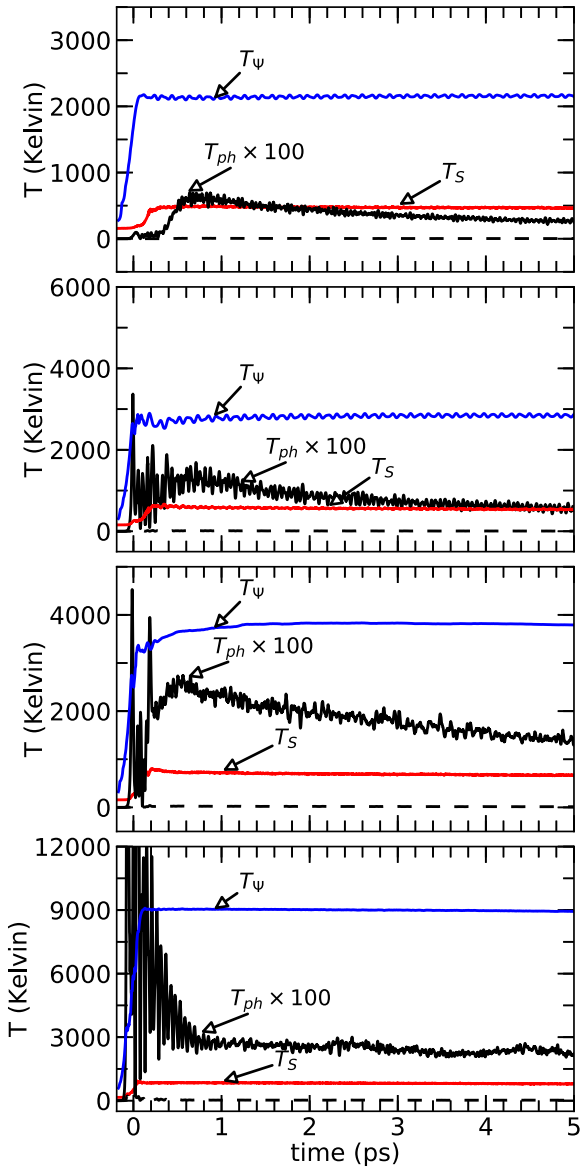

FIG. 28. Temperatures of the electron (blue), spin (red), and phonon (black) subsystems as function of time. The phonon temperatures are scaled by 100. From top to bottom are the representative examples from regime I to IV, i.e., $A_0 = 0.20,\ 0.45,\ 0.53$ and 2.50.

The occupations for different time slices and for the four regimes are shown in Fig. 29. Initially, that is 0.2 ps after the maximum of the light pulse, the occupations do not lie on a continuous function of the one-particle energies but scatter wildly. This is expected because the occupations of the electron states are dominated by the ground-state occupations, the photon energy, and the dipole matrix elements.

Already after an initial period of about 0.5 ps after the pulse maximum, the occupations form a continuous function of the energy. This indicates that the thermalization between electrons of the same energy is very efficient. This result is specific to the choice of one-particle orbitals and energies, namely, the Born-Oppenheimer states.

However, on the timescale of our simulation, the system does not approach a Fermi distribution. Rather, occupations of electrons further away from the chemical potential deviate further from integral occupations than a Fermi distribution: the electrons further away from the Fermi level seem to be "hotter" than those close to the Fermi level. Surprisingly, the tails of the distribution become even flatter with time, that is, they seem to deviate even further from a Fermi distribution.

We attribute this behavior to the strong coupling between different subsystems: Due to the dynamics of the spin and phonon systems, the electrons experience a time-dependent Hamiltonian, that constantly drives the electrons out of their equilibrium distribution. For the one-particle basis $|\phi_j^{\mathrm{BO}}(t)\rangle$ used here, the approach to a Fermi distribution is not a requirement.

2. Cold-plasma model

On the picosecond timescale after an excitation, we find a large disparity between the high temperature of the electrons on the one hand and the low temperatures of spins and phonons on the other hand. This suggests that the optically accessed states are the result of thermodynamic equilibrium of the electron system alone. A quasiequilibrium state such as this has been assumed earlier [14].

In order to test this conjecture, we investigated the phase diagram by increasing the temperature of the electrons, while spins and phonons are kept at zero temperature. That is, spins and phonons are optimized for each electron temperature. The lattice constants are kept equal to the values before excitation because they are usually too slow on the short timescale under consideration.

As shown in Fig. 30, we find four different temperature ranges, which, however, do not directly correspond to the ranges of different excitation behavior.

(i) For $T < T_1$ with $T_1 \approx 2500$ K, we obtain the charge-ordered phase with CE-type magnetic order. Charge-order correlations and the corresponding Jahn-Teller distortions on the central site vanish at T_1 with an approximate square-root behavior $\sim(T_1 - T)^\alpha$ with $0 < \alpha < 1$.

(ii) $T_1 < T < T_2$ with $T_2 = 4200$ K: At $T = T_1$ the charge and orbital orders are completely lost, and the system transforms abruptly from the CE-type antiferromagnetic structure into a ferromagnet. The system is a pure ferromagnet only at $T = T_1$. For $T > T_1$ the spin angle ϕ_c between adjacent *ab* planes increases with an approximate square-root-like behavior toward increasing temperatures, i.e., $\phi_c \sim (T - T_1)^\beta$ with $0 < \beta < 1$. The spin orientation alternates between two values from plane to plane.

(iii) $T_2 < T < T_3$ with $T_3 = 5000$ K: At $T = T_2$, the spins in the *ab* planes become noncollinear. The angle ϕ_{ab} between adjacent spins in the *ab* plane increases approximately linearly from 0° to 180° as the temperature is raised from $T = T_2$ to $T = T_3$.

(iv) $T > T_3$: At $T = T_3$, both spin angles ϕ_{ab} and ϕ_c are 180°, which corresponds to the G-type magnetic order. This is the favorable high-temperature phase for the temperature range explored.

It is important to note that the phase diagram described here has little to do with the equilibrium phase diagram of the material. The phases described above are extreme nonequilibrium states because spins and phonons are at $T = 0$.

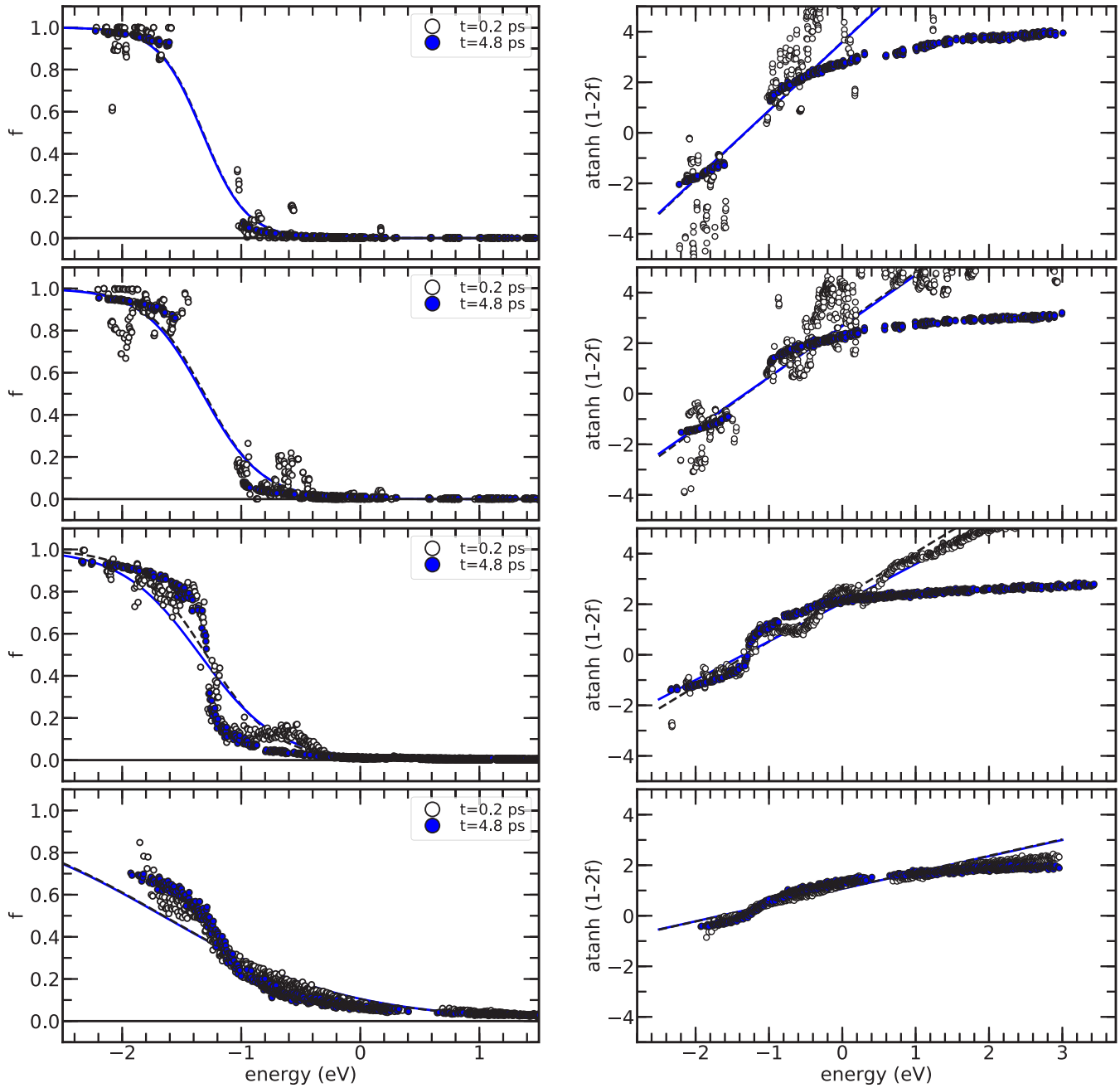

FIG. 29. Distributions of electron occupations $\bar{f}$ at different times, namely, $t = 0.2$ ps (open circles) and 4.8 ps (blue filled circles). From top to bottom are the representative examples from regime I to IV, i.e., $A_0 = 0.20,\ 0.45,\ 0.53$, and $2.50\ \hbar/(ea_0)$. The left figure shows the occupations (circles) versus Born-Oppenheimer energy ϵ_j^{BO}. The dashed black line is the Fermi distributions at 0.2 ps obtained from the energy and particle-number sum rules. The full blue line is the Fermi distribution at 4.8 ps. On the right, the occupations $\bar{f}$ are transformed by $\mathrm{arctanh}(1-2\bar{f})$ which maps a Fermi distribution to a straight line with slope $1/(k_B T_\psi)$ and zero μ_ψ.

We can identify the excitation regimes I and II with the temperature range $T < T_1$. The ferromagnetic state obtained in regime III can be attributed to the range $T_1 < T < T_2$. A nonzero spin angle ϕ_c between the ferromagnetic planes has not been apparent in our time-dependent simulation. We expect this to be a fluctuating quantity that is averaged out.

In regime IV, we find configurations which are noncollinear in the *ab* plane. Interestingly, the noncollinear state with $\phi_{ab} = 90^\circ$ shown in Fig. 25 is a typical state obtained for a range of fluences, while in Fig. 30 it is just one point in a region with continuously changing angles ϕ_{ab}. At even higher fluences, also the G-type structure is encountered.

V. SUMMARY

The optical excitation of half-doped $Pr_{0.5}Ca_{0.5}MnO_3$ has been simulated to study the physical interplay between electronic, spin, and lattice degrees of freedom in response to

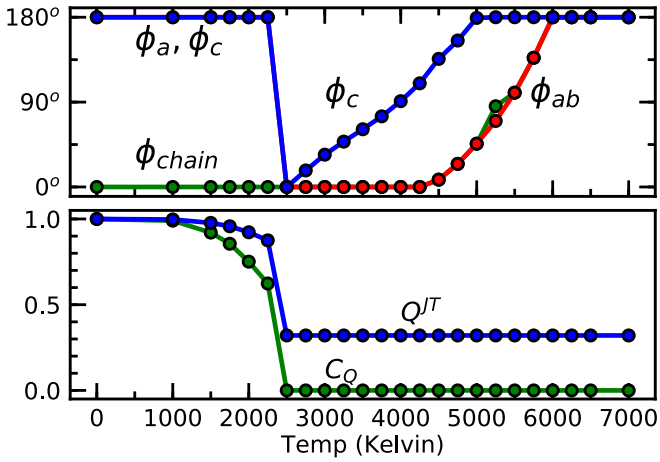

FIG. 30. Nonequilibrium phase diagram with hot electrons and cold spins and phonons. Top: spin angles. ϕ_c is the spin angle between spins in the c direction of the *Pbnm* setting. ϕ_{ab} is the spin angle of neighboring Mn sites in the ab plane. Below $T = T_1$, the angle ϕ_{ab} is replaced by one angle ϕ_a perpendicular to the zigzag chains of the CE-magnetic structure and ϕ_{chain} is the angle within the zigzag chains. Bottom figure: charge-order correlation function C_Q and Jahn-Teller distortion Q^{JT} of the central site as function of temperature. Both are divided by their zero-temperature value.

a femtosecond light pulse. The simulations use Ehrenfest dynamics, in which electrons and spins follow the time-dependent Schrödinger equation while the nuclei proceed on a classical trajectory.

Femtosecond excitations with various intensities and pulse lengths are studied. The pulse acts on the charge-ordered, low-temperature phase with CE-type antiferromagnetism. Four different intensity regimes with qualitative different behavior could be identified.

(1) In regime I, the electron-band structure remains essentially rigid. The electron-hole distribution excitation transfers weight from the central Mn ions of the zigzag chain to the corner sites. The dipole oscillations shuffle charge between two adjacent corner sites. Two coherent phonons with long lifetime are excited as result of the electron-phonon coupling.

(2) In regime II, the spins react and rearrange into short-lived A-type antiferromagnetic structure. The ground-state CE-type antiferromagnetic structure is recovered within a picosecond. The coherent phonons, present also in regime I, survive this transition.

(3) In regime III, charge and orbital orders are destroyed within a few hundred femtoseconds and a ferromagnet is formed. In contrast to regimes I and II, the coherent phonons are damped out rapidly. Due to spin conservation, the ferromagnet is not directly accessible. Rather, an A-type antiferromagnet is formed, which evolves over several picoseconds into a ferromagnet having domains compatible with the size of our simulation cell.

(4) In regime IV, charge and orbital orders are immediately destroyed as in regime III, but now a G-type antiferromagnet is formed rather than an A-type antiferromagnet. Over time, the system evolves into a new noncollinear spin structure with neighboring spins having 90° angles in the ab plane.

The transient magnetic state observed in regime II may shed light onto the thermal Néel transition of $Pr_{1/2}Ca_{1/2}MnO_3$ at 175 K. In regime II, the system maintains the orbital and charge order, but it modifies the spin correlations of neighboring zigzag chains of the CE-type spin structure in the ab plane. Analogously, the Néel transition may be due to a melting of the antiferromagnetic correlations between the zigzag chains, while maintaining the ferromagnetic order within the chains. When the ferromagnetic order within the chains melts at higher temperature, the integrity of the chains with their orbital and charge order is destroyed as in regimes III and IV.

The long lifetime of the magnetic orders in regimes III and IV may qualify for the concept of "hidden phases." Hidden phases [4] are states with unique order which can not be accessed thermodynamically. It must be noted, however, that the timescales covered in our simulations are short compared to those studied experimentally.

In order to make contact with thermodynamics, we estimated the temperatures of the individual subsystems, namely, electrons, spins, and phonons. The temperature of the electronic subsystem raises quickly to several thousand Kelvin, while phonon and spin degrees of freedom remain relatively "cold." An exception are the coherent phonon modes, which initially reach the temperature of the electrons before dissipating their energy into other degrees of freedom.

Following this concept of hot electrons and cold phonons and spins, we have been able to identify the phases accessed by optical excitation with those obtained by raising only the electron temperature.

ACKNOWLEDGMENTS

Funded by the Deutsche Forschungsgemeinschaft (DFG, German Research Foundation) (SFB1073, Grant No. 217133147) through projects B02, B03, and C03. We are grateful to M. T. Brink, S. Manmana, and S. Kehrein for fruitful discussions.

APPENDIX A: NUMERICAL INTEGRATION OF TIME-DEPENDENT SCHRÖDINGER EQUATION

To solve the time-dependent Schrödinger equation for wave functions and spinors, we use the second-order differencing scheme proposed by Askar and Cakmak [54,55].

Given the wave function $|\psi(0)\rangle$ at time $t = 0$ and the time-dependent Hamiltonian $\hat{H}(t)$, the wave function $|\psi(t)\rangle$ can be obtained as $|\psi(t)\rangle = \hat{U}(t, 0)|\psi(0)\rangle$ using the propagator

$$\hat{U}(t', t) = \mathcal{T}_D \exp\left(-\frac{i}{\hbar}\int_t^{t'} d\tau\, \hat{H}(\tau)\right). \tag{A1}$$

$\mathcal{T}_D$ is Dyson's time-ordering operator [56], which rearranges all operators in a product into ascending time order from right to left.

With the time step Δ, subsequent wave functions of a time sequence are related by

$$\begin{aligned}|\psi_n(\Delta)\rangle - |\psi_n(-\Delta)\rangle &= (\hat{U}(\Delta, 0) - \hat{U}(-\Delta, 0))|\psi_n(0)\rangle \\ &= -\frac{2i\Delta}{\hbar}\hat{H}(0)|\psi_n(0)\rangle + O(\Delta^3).\end{aligned} \tag{A2}$$

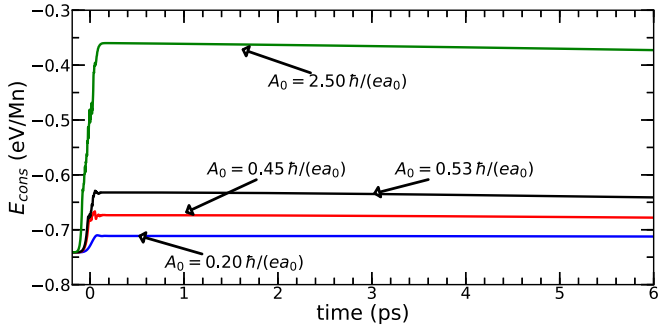

FIG. 31. Energy conservation for three intensities of the excitation. The initial rise is due to the excitation. The largest violation of energy conservation is a slow dissipation of the quantum systems.

The error is reduced by splitting off the dynamical phase using the corresponding energy expectation value $E_n(t) := \langle\psi_n(t)|\hat{H}(t)|\psi_n(t)\rangle$:

$$e^{\frac{i\Delta}{\hbar}E_n(0)}|\psi_n(\Delta)\rangle - e^{-\frac{i\Delta}{\hbar}E_n(0)}|\psi_n(-\Delta)\rangle = -\frac{2i\Delta}{\hbar}(\hat{H}(0) - E_n(0))|\psi_n(0)\rangle + O(\Delta^3). \quad \text{(A3)}$$

This leads to the following iterative scheme:

$$|\psi_n(t+\Delta)\rangle = |\psi(t-\Delta)\rangle e^{-\frac{2i\Delta}{\hbar}E_n(t)} - \frac{2i\Delta}{\hbar}(\hat{H}(t) - E_n(t))|\psi(t)\rangle e^{-\frac{i\Delta}{\hbar}E_n(t)} + O(\Delta^3). \quad \text{(A4)}$$

These equations of motion are time-inversion symmetric per construction.

However, the equations of motion produce aside from the correct solution also a spurious partial solution which changes sign in each iteration. This implies that, over time, the wave function will pick up a contribution from the spurious solution. In order to purify the solution, we interrupt the simulation at regular time intervals and perform a correction step. In the correction step, we filter out the spurious partial solution

$$|\psi'(t)\rangle = |\psi(t)\rangle + \tfrac{1}{4}(|\psi(t+\Delta)\rangle e^{\frac{i}{\hbar}E_n(t)\Delta} - 2|\psi(t)\rangle + |\psi(t-\Delta)\rangle e^{-\frac{i}{\hbar}E_n(t)\Delta}) \quad \text{(A5)}$$

and perform a Gram-Schmidt orthonormalization on the one-particle wave functions for the two subsequent time steps used in the next iteration. We use a time step of $\Delta \approx 10^{-3}$ fs. Correction steps are performed every 20 time steps. The energy conservation is shown in Fig. 31 for different light amplitudes A_0.

APPENDIX B: SPIN DYNAMICS

The dynamics of the spins $\vec{S}_R$ describing the t_{2g} electrons requires special attention. While the spin dynamics is intrinsically of quantum nature, we want to keep all three t_{2g} electrons of a given Mn ion strictly collinear. For this purpose, we map the spin vector $\vec{S}_i$ onto a normalized, complex-valued, two-component spinor $\binom{a_{\uparrow,R}}{a_{\downarrow,R}}$ such that

$$\vec{S}_R = \frac{3\hbar}{2}\begin{pmatrix} a^*_{\uparrow,R}a_{\downarrow,R} + a^*_{\downarrow,R}a_{\uparrow,R} \\ -ia^*_{\uparrow,R}a_{\downarrow,R} + ia^*_{\downarrow,R}a_{\uparrow,R} \\ a^*_{\uparrow,R}a_{\uparrow,R} - a^*_{\downarrow,R}a_{\downarrow,R} \end{pmatrix}. \quad \text{(B1)}$$

The magnetic moment $\vec{m}_S$ of the t_{2g} shell is antiparallel to its spin direction, namely, $\vec{m}_S = -m_S(\frac{3\hbar}{2})^{-1}\vec{S}$. The scalar $m_S := |\vec{m}_S|$ is defined as the absolute value of the magnetic moment.

The equation of motion is derived from the Lagrangian

$$\mathcal{L} = i\hbar\sum_{\sigma,\alpha,R,n} f_n\psi^*_{\sigma,\alpha,R,n}\dot{\psi}_{\sigma,\alpha,R,n} + i\hbar\sum_{\sigma,R} a^*_{\sigma,R}\dot{a}_{\sigma,R} + \frac{1}{2}\sum_{j=1}^{N_O} M_O\dot{R}_j^2 - E_{\text{pot}}[\psi, S[a], R]. \quad \text{(B2)}$$

The spinors $(a_{\uparrow,R}, a_{\downarrow,R})$ evolve under the time-dependent Schrödinger equation

$$i\hbar\partial_t\begin{pmatrix} a_{\uparrow,R} \\ a_{\downarrow,R}\end{pmatrix} = m_S\begin{pmatrix} B_{z,R} & B_{x,R} - iB_{y,R} \\ B_{x,R} + iB_{y,R} & -B_{z,R}\end{pmatrix}\begin{pmatrix} a_{\uparrow,R} \\ a_{\downarrow,R}\end{pmatrix} \quad \text{(B3)}$$

with

$$m_S\vec{B}_R = \left(\frac{3\hbar}{2}\right)^{-1} J_{\text{AF}}\sum_{R'\in NN_R}\vec{S}_{R'} - J_{\text{Hund}}\sum_{\alpha}\begin{pmatrix} \rho_{\downarrow,\alpha,R,\uparrow,\alpha,R} + \rho_{\uparrow,\alpha,R,\downarrow,\alpha,R} \\ -i\rho_{\downarrow,\alpha,R,\uparrow,\alpha,R} + i\rho_{\uparrow,\alpha,R,\downarrow,\alpha,R} \\ \rho_{\uparrow,\alpha,R,\uparrow,\alpha,R} - \rho_{\downarrow,\alpha,R,\downarrow,\alpha,R}\end{pmatrix}. \quad \text{(B4)}$$

The summation index $R' \in NN_R$ runs over nearest-neighbor sites of site R. The first term in Eq. (B4) describes the antiferromagnetic coupling with neighboring spins. The second term in Eq. (B4) describes Hund's coupling between t_{2g} and e_g electrons on the same site. J_{AF} is the antiferromagnetic spin-coupling parameter and J_{Hund} is the Hund's coupling parameter.

The dynamical equation (B3) is equivalent to

$$\partial_t\vec{S}_R = \frac{2m_S}{\hbar}\vec{B}_R \times \vec{S}_R, \quad \text{(B5)}$$

where $\times$ denotes the vector product.

APPENDIX C: STRAIN DYNAMICS

In this study, the scale factors g_x, g_y, and g_z are dynamical variables, which describe long-wavelength acoustic modes that are responsible for the strain effects in manganites [45,46]. We enforce $g_x = g_y$.

In order to describe the sound wave observed in experiment, we introduce a classical kinetic energy $\frac{1}{2}M_g\sum_{m=1}^{3}\dot{g}_m^2$, which determines the Newton's equations of motion for the scale factors g_m. In thin-film experiments, the wave vector of a sound wave perpendicular to the film is quantized, which results in a standing wave with a characteristic frequency. The sound wave modulates the optical density of the material,

which can be detected by the optical absorption measurements [13–15].

We adjusted the fictitious mass M_g to simulate this effect. In our model, a sound wave is excited in a material without e_g electrons with $\vec{q} = 0$ and with polarization along the c direction. M_g is chosen so that our model material oscillates with the same frequency as the film in experiment [7], namely, ≈25 GHz.

APPENDIX D: PEIERLS SUBSTITUTION

In this Appendix, we give a brief derivation of the Peierls-substitution method [23,24]. The electric field $\vec{E} = -\partial_t \vec{A}$ of the light pulse is expressed by a vector potential

$$\vec{A}(\vec{r},t) = \frac{\vec{e}_A}{2}(A_0 e^{i(\vec{k}\vec{r}-\omega t)} + A_0^* e^{-i(\vec{k}\vec{r}-\omega t)})g(t), \tag{D1}$$

where $\vec{e}_A$ is the polarization direction of the vector potential and $g(t)$ is an envelope function, which is normalized so that

$$\int dt\ |g(t)|^2 = 1. \tag{D2}$$

The electrons experience a Hamiltonian of the form

$$\hat{H}[\vec{A}] = \frac{1}{2m_e}(\hat{\vec{p}} - q\vec{A}(\hat{\vec{r}},t))^2 + V(\hat{\vec{r}}), \tag{D3}$$

where q is the electron charge, m_e its mass, and V is the lattice potential.

The Hamilton matrix elements are evaluated in a basis set of local orbitals centered at positions $\vec{R}_\alpha$, that have the vector potential explicitly built in. From a regular basis set of local orbitals $|\chi_\alpha\rangle$, field-dependent basis functions

$$\langle\vec{r}|\tilde{\chi}_\alpha\rangle = \exp\left[\frac{i}{\hbar}q\int_{\vec{R}_\alpha}^{\vec{r}} d\vec{r}'\vec{A}(\vec{r}',t)\right]\langle\vec{r}|\chi_\alpha\rangle \tag{D4}$$

are constructed [23,24]. The integral of the vector potential is path dependent: we choose a straight line from the central atom $\vec{R}_\alpha$ to the position $\vec{r}$.

Substituting the above ansatz (D4), we obtain

$$\begin{aligned}&\langle\vec{r}|(\hat{\vec{p}} - q\vec{A}(\hat{\vec{r}},t))|\tilde{\chi}_\alpha\rangle \\ &\quad= \exp\left[\frac{i}{\hbar}q\int_{\vec{R}_\alpha}^{\vec{r}} d\vec{r}'\vec{A}(\vec{r}',t)\right]\langle\vec{r}|\hat{\vec{p}}|\chi_\alpha\rangle.\end{aligned} \tag{D5}$$

From Eqs. (D3) and (D5), we obtain

$$\langle\tilde{\chi}_\alpha|\hat{H}|\tilde{\chi}_\beta\rangle = e^{-i\Phi_{\alpha,\beta}(t)}\langle\chi_\alpha|e^{\frac{i}{\hbar}q\mathcal{F}_{\alpha,\beta}(\hat{\vec{r}},t)}\hat{H}|\chi_\beta\rangle, \tag{D6}$$

where

$$\Phi_{\alpha,\beta}(t) := \frac{q}{\hbar}\int_{\vec{R}_\alpha}^{\vec{R}_\beta} d\vec{r}'\vec{A}(\vec{r}',t) \tag{D7}$$

is the Peierls phase. Furthermore, we define the small quantity $\mathcal{F}_{\alpha,\beta}(\vec{r},t)$, which appears in the above Eq. (D6), as

$$\begin{aligned}\mathcal{F}_{\alpha,\beta}(\vec{r},t) := &\int_{\vec{R}_\alpha}^{\vec{R}_\beta} d\vec{r}'\vec{A}(\vec{r}',t) + \int_{\vec{R}_\beta}^{\vec{r}} d\vec{r}'\vec{A}(\vec{r}',t) \\ &+ \int_{\vec{r}}^{\vec{R}_\alpha} d\vec{r}'\vec{A}(\vec{r}',t),\end{aligned} \tag{D8}$$

$\mathcal{F}_{\alpha,\beta}(\vec{r},t)$ is a magnetic flux through triangle with corners at $\vec{R}_\alpha$, $\vec{R}_\beta$, and $\vec{r}$.

The time-dependent Schrödinger equation for a wave function $|\psi_n(t)\rangle = \sum_\beta |\tilde{\chi}_\beta(t)\rangle c_{\beta,n}(t)$ obtains the form

$$\sum_\beta e^{-i\Phi_{\alpha,\beta}(t)}[\tilde{O}_{\alpha,\beta}(t)i\hbar\partial_t - \tilde{H}_{\alpha,\beta}(t)]c_{\beta,n}(t) = 0 \tag{D9}$$

with

$$\begin{aligned}\tilde{H}_{\alpha,\beta}(t) &:= \langle\chi_\alpha|e^{\frac{i}{\hbar}\mathcal{F}_{\alpha,\beta}(\hat{\vec{r}},t)}\left(\hat{H}[\vec{0}] + q\int_{\vec{R}_\beta}^{\vec{r}} d\vec{r}'\dot{\vec{A}}(\vec{r}',t)\right)|\chi_\beta\rangle, \\ \tilde{O}_{\alpha,\beta}(t) &:= \langle\chi_\alpha|e^{\frac{i}{\hbar}\mathcal{F}_{\alpha,\beta}(\hat{\vec{r}},t)}|\chi_\beta\rangle.\end{aligned} \tag{D10}$$

In this form, the Peierls substitution method [23] is formally exact. In practice, $\mathcal{F}_{\alpha,\beta}(\vec{r},t)$ is neglected. For this to be a good approximation, the basis set needs to be sufficiently localized.

Furthermore, the vector potential is approximated by a constant. This is equivalent to the long-wavelength limit. It also excludes dipole-forbidden, but quadrupole-allowed, transitions. The latter are not considered relevant in comparison with the strong charge-transfer transitions in this work.

With these approximations, by exploiting the orthonormality of our basis set, and after ignoring off-site terms of the dipole matrix elements, we obtain

$$\begin{aligned}i\hbar\partial_t c_{\alpha,n} = &\sum_\beta e^{\frac{-iq}{\hbar}\vec{A}(t)(\vec{R}_\beta - \vec{R}_\alpha)}\langle\chi_\alpha|\hat{H}[\vec{0}]|\chi_\beta\rangle c_{\beta,n} \\ &+ \sum_\beta \delta_{R_\alpha,R_\beta}(-q\dot{A}(\vec{t})\langle\chi_\alpha|\vec{r} - \vec{R}_\beta|\chi_\beta\rangle)c_{\beta,n}.\end{aligned} \tag{D11}$$

The first term on the right-hand side describes charge-transfer transitions, while the second term describes dipole-allowed onsite transitions. The latter vanish in our model and are included here only for the sake of completeness.

The Peierls phase only affects off-site matrix elements. In our case, these are the hopping matrix elements. Thus, the only change required to incorporate the excitation is to multiply the hopping matrix elements with the time-dependent Peierls phase.

1. Temperatures

a. Phonon temperature

The temperature T_{ph} of the phonon degrees of freedom has been evaluated from the kinetic energy of Jahn-Teller active and breathing phonon modes of the oxygen ions. We use the relation

$$\sum_{i=1}^{N_O}\frac{1}{2}M_O\dot{\vec{R}}_i^2 = \frac{N_O}{2}k_B T_{ph}, \tag{D12}$$

where index i runs over all N_O oxygen ions in the unit cell and M_O is the mass of the oxygen ion.

There is only one degree of freedom per oxygen atom in our simulation because only three phonon modes per formula unit are considered. These are the modes with strong electron-phonon coupling, which receive the energy directly from the excited electrons and holes. Only later, these "hot" modes

dissipate their energy into the other phonon modes and the spin system.

b. Electron temperature

The temperature of the electronic degrees of freedom are obtained from the occupations of the Born-Oppenheimer wave functions. For that purpose, we extract the one-particle wave functions $|\psi_j(t)\rangle$ and the instantaneous one-particle Hamiltonian $\hat{h}^{\mathrm{BO}}(t)$ acting on the electrons. The Hamiltonian is the Born-Oppenheimer Hamiltonian for the instantaneous spin distribution and atomic positions.

Let $|\phi_j^{\mathrm{BO}}(t)\rangle$ be the eigenstates and $\epsilon_j^{\mathrm{BO}}(t)$ the eigenvalues of the one-particle Hamiltonian $\hat{h}^{\mathrm{BO}}(t)$. The occupations $\bar{f}_j$ of the Born-Oppenheimer states $|\phi_j^{\mathrm{BO}}(t)\rangle$ are obtained from their projections onto the occupied wave functions $|\psi_j(t)\rangle$ as

$$\bar{f}_j(t) := \sum_{n=1}^{N_e} \left|\langle\psi_n(t)|\phi_j^{\mathrm{BO}}(t)\rangle\right|^2. \tag{D13}$$

Electron temperature T_ψ and electron chemical potential μ are determined such that energy and particle numbers coincide with those of a thermal distribution, i.e.,

$$\begin{aligned}\sum_j \bar{f}_j &= \sum_j \left(e^{(\epsilon_j^{\mathrm{BO}}-\mu)/(k_B T_\psi)}+1\right)^{-1},\\ \sum_j \bar{f}_j \epsilon_j^{\mathrm{BO}} &= \sum_j \left(e^{(\epsilon_j^{\mathrm{BO}}-\mu)/(k_B T_\psi)}+1\right)^{-1}\epsilon_j^{\mathrm{BO}}.\end{aligned} \tag{D14}$$

In order to compare the instantaneous distributions $(\bar{f}_j, \epsilon_j)$ to the Fermi distribution $f_{T,\mu}(\epsilon) = 1/\{1+\exp[\frac{1}{k_B T}(\epsilon-\mu)]\}$, we will plot

$$z(\bar{f}) = \operatorname{arctanh}(1-2\bar{f}) \tag{D15}$$

because this transforms a Fermi distribution into a linear function of the energy:

$$z(f_{T,\mu}(\epsilon)) = \frac{1}{k_B T}(\epsilon-\mu). \tag{D16}$$

As a result, we can read the quasitemperature from the slope and the quasi-Fermi level from the zero of the interpolated line through the data points $(z(\bar{f}_j), \epsilon_j^{\mathrm{BO}})$.

c. Temperature of the spin subsystem

We extract the temperature of the spin subsystem, i.e., the spins of the t_{2g} electrons, analogously to that of the e_g electrons. For each time step, we extract a Born-Oppenheimer Hamiltonian

$$\mathbf{h}_R^{\mathrm{BO},S} := m_S \begin{pmatrix} B_{z,R} & B_{x,R}-iB_{y,R} \\ B_{x,R}+iB_{y,R} & -B_{z,R}\end{pmatrix} \tag{D17}$$

with $\vec{B}_R$ defined in Eq. (B4) and the absolute value m_S of the t_{2g} magnetic moment.

The projections of the instantaneous Pauli spinors $\vec{a}_R(t)$ onto the eigenvectors $\vec{a}_{j,R}^{\mathrm{BO}}(t)$ of $\mathbf{h}_R^{\mathrm{BO},S}(t)$ yield occupations

$$\tilde{f}_{j,R}(t) = \left|\sum_{\sigma\in\{\uparrow,\downarrow\}} a_{\sigma,R}^*(t) a_{\sigma,j,R}^{\mathrm{BO}}(t)\right|^2 \tag{D18}$$

for ground state with $j=0$ and excited state with $j=1$.

The comparison with the internal energy for noninteracting spins in an external magnetic field provides a relation

$$\sum_R (\tilde{f}_{0,R}-\tilde{f}_{1,R}) = \sum_R \tanh\left(\frac{m_S|\vec{B}_R|}{k_B T_S}\right) \tag{D19}$$

which is resolved for the instantaneous temperature $T_S(t)$ of the spin system.

A more detailed derivation of the expressions summarized here is provided in Appendix E.

APPENDIX E: TEMPERATURE OF THE SPIN SUBSYSTEM

The temperature of the spin system is extracted analogously to that of the electrons. We consider a system of uncoupled spins in a magnetic-field distribution $\vec{B}_R$ defined by the local Born-Oppenheimer Hamiltonian for the spin system according to Eq. (D17). The free energy of this system is

$$F_T = -k_B T \ln \sum_{\vec{\sigma}} e^{-\frac{1}{k_B T}E_{\vec{\sigma}}}, \tag{E1}$$

where the energy of a spin distribution $\vec{\sigma}$ is

$$E_{\vec{\sigma}} = -\sum_R m_S|\vec{B}_R|(-1)^{\sigma_R}. \tag{E2}$$

$\sigma_R \in \{0,1\}$ characterizes the ground and excited states of the local spin $\vec{S}_R$ of the t_{2g} electrons at site R. The absolute value of the magnetic moment related to the spin $\vec{S}_R$ of the three t_{2g} electrons at a given site is $m_S = |\gamma\frac{3\hbar}{2}|$.

This yields for the free energy

$$F_T = -k_B T \sum_R \ln\left[2\cosh\left(\frac{m_S|\vec{B}_R|}{k_B T}\right)\right]. \tag{E3}$$

The instantaneous temperature of the spin system is extracted by comparing the energy obtained from the instantaneous spin distribution

$$E(t) = \sum_R \vec{a}_R^*(t)\mathbf{h}_R^{\mathrm{BO},S}(t)\vec{a}_R(t) \tag{E4}$$

with the energy $\langle E\rangle_T = \beta\partial_\beta F_T$ of the thermal ensemble, where $\beta = 1/(k_B T)$.

With the eigenstates $\vec{a}_{j,R}^{\mathrm{BO}}$ and the eigenvalues $\tilde{\epsilon}_{j,R}$ of the Born-Oppenheimer Hamiltonian $\mathbf{h}_R^{\mathrm{BO},S}$, the instantaneous energy equation (E4) is

$$E(t) = \sum_R \tilde{f}_{j,R}(t)\tilde{\epsilon}_{j,R}(t) \tag{E5}$$

with occupations

$$\tilde{f}_{j,R}(t) = \left|\vec{a}_R^*(t)\vec{a}_{j,R}^{\mathrm{BO}}(t)\right|^2 \tag{E6}$$

for the local ground state with $j=0$ and the excited state with $j=1$.

The requirement

$$\sum_R \sum_{j=0}^{1} \tilde{f}_{j,R}\tilde{\epsilon}_{j,R} \stackrel{!}{=} \beta\partial_\beta F_\beta = \langle E\rangle_T \tag{E7}$$

provides an expression for the instantaneous temperature $T(t)$:

$$\sum_R (\tilde{f}_{0,R} - \tilde{f}_{1,R}) = \sum_R \tanh\left(\frac{m_S|\vec{B}_R|}{k_B T}\right). \tag{E8}$$

APPENDIX F: FREQUENCIES OF THE COHERENT PHONON MODES

The frequencies of the coherent modes, present in regimes I and II, have been extracted by nonlinear curve fitting of a superposition of a constant and two cosine functions with amplitude, frequency, and phase shift as variable parameters. The quality of the fit is shown in Fig. 32. The fit gives a frequency of 9.7 and 15.7 THz.

The vibration of 15.7 THz is dominant in the Δd_y^{4+} and can be attributed to the planar breathing mode on the corner sites of the CE-type magnetic structure, which couples to the charge transfer from the central to the corner sites. The lower frequency with $\nu = 9.7$ THz is a Jahn-Teller mode on the central site of a trimer.

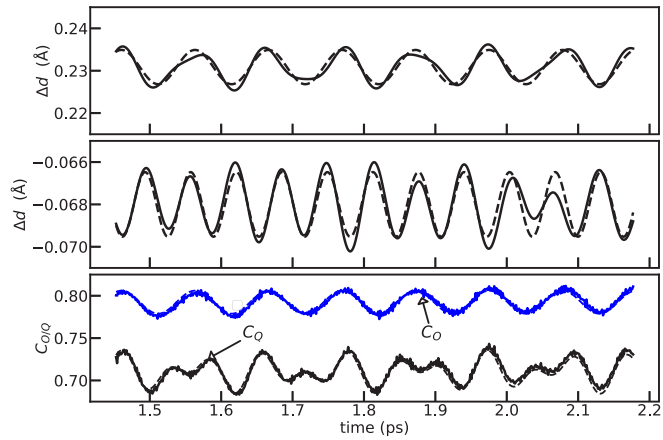

FIG. 32. Fit of the phonon modes and diffraction intensities. The top figure shows $\Delta d_\parallel^{3+}$ (red) and the fit (dashed). The middle graph shows Δd_y^{4+} and its fit. The bottom graph shows the correlation functions C_Q for charge and C_O for orbital order and their fits. The derived frequencies are 9.7 and 15.7 THz. The trajectory has been performed for a light amplitude of $A_0 = 0.20\ \hbar/(ea_0)$.

In order to confirm that the oscillations of the charge- and orbital-order correlation functions are a direct consequence of the coherent phonons, the correlation functions have been fitted with same two frequencies. The perfect agreement shown in Fig. 32 supports our conjecture.

[1] Y. H. Ren, M. Ebrahim, H. B. Zhao, G. Lüpke, Z. A. Xu, V. Adyam, and Q. Li, Phys. Rev. B **78**, 014408 (2008).
[2] M. Matsubara, Y. Okimoto, T. Ogasawara, Y. Tomioka, H. Okamoto, and Y. Tokura, Phys. Rev. Lett. **99**, 207401 (2007).
[3] T. Ogasawara, M. Matsubara, Y. Tomioka, M. Kuwata-Gonokami, H. Okamoto, and Y. Tokura, Phys. Rev. B **68**, 180407(R) (2003).
[4] H. Ichikawa, S. Nozawa, T. Sato, A. Tomita, K. Ichiyanagi, M. Chollet, L. Guerin, N. Dean, A. Cavalleri, S. ichi Adachi, T. hisa Arima, H. Sawa, Y. Ogimoto, M. Nakamura, R. Tamaki, K. Miyano, and S. ya Koshihara, Nat. Mater. **10**, 101 (2011).
[5] M. Rini, R. Tobey, N. Dean, J. Itatani, Y. Tomioka, Y. Tokura, R. W. Schoenlein, and A. Cavalleri, Nature (London) **449**, 72 (2007).
[6] D. Polli, M. Rini, S. Wall, R. W. Schoenlein, Y. Tomioka, Y. Tokura, G. Cerullo, and A. Cavalleri, Nat. Mater. **6**, 643 (2007).
[7] D. Raiser, S. Mildner, B. Ifland, M. Sotoudeh, P. Blöchl, S. Techert, and C. Jooss, Adv. Energy Mater. **7**, 1602174 (2017).
[8] R. P. Prasankumar, S. Zvyagin, K. V. Kamenev, G. Balakrishnan, D. M. Paul, A. J. Taylor, and R. D. Averitt, Phys. Rev. B **76**, 020402(R) (2007).
[9] R. D. Averitt, A. I. Lobad, C. Kwon, S. A. Trugman, V. K. Thorsmølle, and A. J. Taylor, Phys. Rev. Lett. **87**, 017401 (2001).
[10] K. H. Wu, T. Y. Hsu, H. C. Shih, Y. J. Chen, C. W. Luo, T. M. Uen, J.-Y. Lin, J. Y. Juang, and T. Kobayashi, J. Appl. Phys. **105**, 043901 (2009).
[11] J. Bielecki, R. Rauer, E. Zanghellini, R. Gunnarsson, K. Dörr, and L. Börjesson, Phys. Rev. B **81**, 064434 (2010).
[12] H. Lin, H. Liu, L. Lin, S. Dong, H. Chen, Y. Bai, T. Miao, Y. Yu, W. Yu, J. Tang, Y. Zhu, Y. Kou, J. Niu, Z. Cheng, J. Xiao, W. Wang, E. Dagotto, L. Yin, and J. Shen, Phys. Rev. Lett. **120**, 267202 (2018).
[13] C. Thomsen, J. Strait, Z. Vardeny, H. J. Maris, J. Tauc, and J. J. Hauser, Phys. Rev. Lett. **53**, 989 (1984).
[14] H. J. Zeiger, J. Vidal, T. K. Cheng, E. P. Ippen, G. Dresselhaus, and M. S. Dresselhaus, Phys. Rev. B **45**, 768 (1992).
[15] K.-J. Jang, J. Lim, J. Ahn, J.-H. Kim, K.-J. Yee, and J. S. Ahn, Phys. Rev. B **81**, 214416 (2010).
[16] M. Sotoudeh, S. Rajpurohit, P. Blöchl, D. Mierwaldt, J. Norpoth, V. Roddatis, S. Mildner, B. Kressdorf, B. Ifland, and C. Jooss, Phys. Rev. B **95**, 235150 (2017).
[17] J. C. Tully, Faraday Discuss. **110**, 407 (1998).
[18] E. Dagotto, T. Hota, and A. Moreo, Phys. Rep. **344**, 1 (2001).
[19] T. Hotta and E. Dagotto, *Colossal Magnetoresistive Manganites*, edited by T. Chatterji (Springer, Netherlands, 2004), pp. 207-262.
[20] T. Hotta, Rep. Prog. Phys. **69**, 2061 (2006).
[21] E. Müller-Hartmann and E. Dagotto, Phys. Rev. B **54**, R6819 (1996).
[22] A. McLachlan, Mol. Phys. **8**, 39 (1964).
[23] R. Peierls, Z. Phys. **80**, 763 (1933).
[24] D. R. Hofstadter, Phys. Rev. B **14**, 2239 (1976).
[25] D. Feil, Isr. J. Chem. **16**, 103 (1977).

[26] T. Hotta and E. Dagotto, Phys. Rev. B **61**, R11879 (2000).
[27] E. O. Wollan and W. C. Koehler, Phys. Rev. **100**, 545 (1955).
[28] J. B. Goodenough, Phys. Rev. **100**, 564 (1955).
[29] Z. Jirak, S. Krupicka, Z. Simsa, M. Dlouha, and S. Vratislav, J. Magn. Magn. Mater. **53**, 153 (1985).
[30] M. v. Zimmermann, C. S. Nelson, J. P. Hill, D. Gibbs, M. Blume, D. Casa, B. Keimer, Y. Murakami, C.-C. Kao, C. Venkataraman, T. Gog, Y. Tomioka, and Y. Tokura, Phys. Rev. B **64**, 195133 (2001).
[31] J. García, M. C. Sańchez, G. Subías, and J. Blasco, J. Phys.: Condens. Matter **13**, 3229 (2001).
[32] S. Grenier, J. P. Hill, D. Gibbs, K. J. Thomas, M. v. Zimmermann, C. S. Nelson, V. Kiryukhin, Y. Tokura, Y. Tomioka, D. Casa, T. Gog, and C. Venkataraman, Phys. Rev. B **69**, 134419 (2004).
[33] C. Jooss, L. Wu, T. Beetz, R. F. Klie, M. Beleggia, M. A. Schofield, S. Schramm, J. Hoffmann, and Y. Zhu, Proc. Natl. Acad. Sci. USA **104**, 13597 (2007).
[34] D. Mierwaldt, S. Mildner, R. Arrigo, A. Knop-Gericke, E. Franke, A. Blumenstein, J. Hoffmann, and C. Jooss, Catalysts **4**, 129 (2014).
[35] *IUPAC Compendium of Chemical Terminology*, 2nd ed., edited by A. D. McNaught and A. Wilkinson (Blackwell, Oxford, 1997).
[36] S. Mildner, J. Hoffmann, P. E. Blöchl, S. Techert, and C. Jooss, Phys. Rev. B **92**, 035145 (2015).
[37] N. N. Loshkareva, L. V. Nomerovannaya, E. V. Mostovshchikova, A. A. Makhnev, Y. P. Sukhorukov, N. I. Solin, T. I. Arbuzova, S. V. Naumov, N. V. Kostromitina, A. M. Balbashov, and L. N. Rybina, Phys. Rev. B **70**, 224406 (2004).
[38] C. Hartinger, F. Mayr, A. Loidl, and T. Kopp, Phys. Rev. B **73**, 024408 (2006).
[39] M. Quijada, J. Černe, J. R. Simpson, H. D. Drew, K. H. Ahn, A. J. Millis, R. Shreekala, R. Ramesh, M. Rajeswari, and T. Venkatesan, Phys. Rev. B **58**, 16093 (1998).
[40] A. S. Moskvin, A. A. Makhnev, L. V. Nomerovannaya, N. N. Loshkareva, and A. M. Balbashov, Phys. Rev. B **82**, 035106 (2010).
[41] B. Ifland, J. Hoffmann, B. Kressdorf, V. Roddatis, M. Seibt, and C. Jooss, New J. Phys. **19**, 063046 (2017).
[42] D. A. Steck, *Quantum and Atomic Optics* available online at http://steck.us/teaching, revision 0.12.6, 23 April 2019.
[43] P. Beaud, A. Caviezel, S. O. Mariager, L. Rettig, G. Ingold, C. Dornes, S.-W. Huang, J. A. Johnson, M. Radovic, T. Huber, T. Kubacka, A. Ferrer, H. T. Lemke, M. Chollet, D. Zhu, J. M. Glownia, M. Sikorski, A. Robert, H. Wadati, M. Nakamura *et al.*, Nat. Mater. **13**, 923 (2014).
[44] H. Matsuzaki, H. Uemura, M. Matsubara, T. Kimura, Y. Tokura, and H. Okamoto, Phys. Rev. B **79**, 235131 (2009).
[45] D. Lim, V. K. Thorsmølle, R. D. Averitt, Q. X. Jia, K. H. Ahn, M. J. Graf, S. A. Trugman, and A. J. Taylor, Phys. Rev. B **71**, 134403 (2005).
[46] V. Esposito, L. Rettig, E. Abreu, E. M. Bothschafter, G. Ingold, M. Kawasaki, M. Kubli, G. Lantz, M. Nakamura, J. Rittman, M. Savoini, Y. Tokura, U. Staub, S. L. Johnson, and P. Beaud, Phys. Rev. B **97**, 014312 (2018).
[47] J. K. Dewhurst, P. Elliott, S. Shallcross, E. K. U. Gross, and S. Sharma, Nano Lett. **18**, 1842 (2018).
[48] C. Zener, Phys. Rev. **82**, 403 (1951).
[49] P. W. Anderson and H. Hasegawa, Phys. Rev. **100**, 675 (1955).
[50] A. J. Millis, R. Mueller, and B. I. Shraiman, Phys. Rev. B **54**, 5405 (1996).
[51] T. Li, A. Patz, L. Mouchliadis, J. Yan, T. A. Lograsso, I. E. Perakis, and J. Wang, Nature (London) **496**, 69 (2013).
[52] S. Y. Zhou, M. C. Langner, Y. Zhu, Y.-D. Chuang, M. Rini, T. E. Glover, M. P. Hertlein, A. G. C. Gonzalez, N. Tahir, Y. Tomioka, Y. Tokura, Z. Hussain, and R. W. Schoenlein, Sci. Rep. **4**, 4050 (2014).
[53] A. Ono and S. Ishihara, Phys. Rev. Lett. **119**, 207202 (2017).
[54] A. Askar and A. Cakmak, J. Chem. Phys. **68**, 2794 (1978).
[55] R. Kosloff, J. Phys. Chem. **92**, 2087 (1988).
[56] F. J. Dyson, Phys. Rev. **75**, 486 (1949).